Unsteady compressible flow in ducts with varying cross-section: Comparison between the nonconservative Euler system and the axisymmetric flow model

D. Rochette [a], S. Clain [b,*], W. Bussière [c]

[a] Clermont Université, Université Blaise Pascal, LAEPT, BP 10448, F-63000 Clermont-Ferrand, France
[b] Institut de Mathématiques, CNRS UMR 5219, Université Paul Sabatier, F-31062 Toulouse Cedex 4, France
[c] Clermont Université, Université d'Auvergne, LAEPT, BP 10448, F-63000 Clermont-Ferrand, France

ARTICLE INFO

ABSTRACT

Most of nonconservative hyperbolic systems corresponds to a reduction of an initial three-dimensional problem deriving from a homogenization procedure. Unfortunately, the reduced model gives rise to two new difficulties: the resonance problem corresponding to a splitting or a merging of the genuinely nonlinear waves and the non uniqueness of the Riemann problem solution. The question arises to check whether the two problems correspond and provide similar solutions, at least numerically. In this paper, we propose a comparison between the one-dimensional nonconservative Euler equations modelling the duct with variable cross-sectional area with its original three-dimensional conservative Euler system. Based on the classification of the Riemann problems proposed in [13], we compare the numerical results of the two models for a large series of representative configurations. We also propose a new example of non uniqueness for the Riemann problem involving the resonance phenomena.

© 2011 Elsevier Ltd. All rights reserved.

1. Introduction

Since two decades, nonconservative hyperbolic systems have received considerable attention both from a theoretical and a numerical points of view. Usually deriving from a homogenization procedure of an initial three-dimensional model, several problems of physical or engineering importance are governed with a nonconservative hyperbolic system. For instance, the nonconservative Euler equations, as well-named the quasi-one-dimensional Euler in a duct, are obtained by averaging the usual multi-dimensional Euler equations over the duct cross-section [4,32]. We can mention other kinds of nonconservative system, the shallow-water problem with topography [2,8,17–19], the two-layer shallow-water problem [16], the sediment transport [10,30], the multi-fluid models [1,7,31], the Baer–Nunziato system [5] and the compressible gas flow in porous media [6,28,29].

Numerical approximations of the solutions of nonconservative hyperbolic systems have to be cleverly evaluated with specific numerical schemes named well-balanced schemes where the steady-state solutions are numerically preserved [1,12,13,21,22]. A large literature is now devoted on the subject [26,27]. The question we tackle in the article is the correspondence between the numerical solutions of the reduced problem, *i.e.* the nonconservative problem and the numerical solution computed with the initial

problem, *i.e.* the full three-dimensional one. Indeed, nonconservative systems give rise to essentially two new difficulties: the resonance phenomena and the non uniqueness of the solutions [4,12,13,21] whereas such phenomena do not exist at the three-dimensional level: the homogenization procedure looses information and the classical entropy argument (in the Lax sense for instance) is not enough to obtain a unique solution (numerically at least).

Few studies on the comparisons have been realized since such a problem has gained less attention and most of them only concern the shallow-water problem [3]. However the question seems of crucial importance for two reasons: firstly we have to check that the solutions of the two problems really correspond (at least numerically) for every type of configuration and secondly we have to select the most physical solution when we face a non uniqueness situation: we have several different entropy solutions (in the Lax sense) with the reduced model for the same Riemann problem and we choose the one which better fit with the three-dimensional solution.

To address the first issue, we deal with the variational cross-section duct problem or equivalently the gas flow in inhomogeneous porous media. We have implemented the scheme proposed in [13] to solve the nonconservative one-dimensional problem and the scheme proposed in [14] to solve the full three-dimensional axisymmetric one. We have numerically experimented all the available configurations proposed in [13] and compared it with their equivalent three-dimensional problem. We aim to prove that all the situations, even the most complex ones like the splitting or

---

* Corresponding author.
   E-mail address: stephane.clain@math.univ-toulouse.fr (S. Clain).

merging of the simple genuinely nonlinear wave across the interface, are reproduced by the initial conservative Euler model which justify the reality of such configurations. The second issue we address concerns the non uniqueness of the solution for the reduced problem. A first example has been proposed by Andrianov and Warnecke [4] where a subsonic solution and a supersonic solution are available for the same Riemann problem. Here, we propose a new non uniqueness case with a more complex situation: a supersonic solution and a resonance solution. Such an example proves that non uniqueness can also arise with complex configurations involving the merging or the splitting of the simple waves.

The organization of the paper is as follows. In Section 2, we present the governing Euler equations in cylindrical coordinates assuming rotational symmetry and the one-dimensional nonconservative Euler equations as well as a short review on the numerical techniques employed to discretize the equations. In Section 3, we present all the admissible configurations for the Riemann problem in a duct with variable cross-section. Section 4 is devoted to the comparison between the exact solutions obtained with the inverse Riemann problem and the numerical approximations obtained by the one-dimensional nonconservative system and the axisymmetric flow model for all the configurations listed in [13]. In the Section 5, we study the non uniqueness of the Riemann problem for the nonconservative system. We propose a new example involving a complex configuration with the resonance phenomenon. Finally, we propose in Section 6 a set of simulations to compare the interaction of a planar shock wave entering in a duct with a rough or a smooth cross-section variation. Concluding remarks are made in Section 7.

2. Gas flow models and numerical methods

Perfect gas flow in variational cross-section is modelled with the three-dimensional axisymmetric Euler system where the cylindrical coordinates are employed to provide a simpler two-dimensional space variables problem with respect to the radial and axial coordinates (r,x). Deriving from the primitive model, a nonconservative one-dimensional model – named the variational cross-section duct model [4] – based on a homogenization with respect to variable r is obtained. Notice that the 1D reduction of the 3D problem is a model and violates the standard conditions allowing to neglect multidimensional effects (large radius of curvature, small variation of the cross-sectional).

The present section is dedicated to a short presentation of the two models and their respective numerical methods. Note that we use the x-axis as symmetry axis instead of the traditional z-axis for the three-dimensional model to provide a natural correspondence with the one-dimensional nonconservative model.

2.1. Euler equations for axisymmetric flows

Let us consider an axisymmetric domain $\Omega \times [0,2\pi[$ obtained by the rotation of a two-dimensional pattern Ω with respect to axis Δ corresponding to the azimuthal coordinate x. Remark that the domain is not cylindrical, *a priori*, since the orthogonal cross-section $S(x)$ may vary with x as presented in Fig. 1.

Using the cylindrical coordinate and assuming a non swirling flow, the Euler equations governing axially symmetric flow of a compressible inviscid perfect gas write as in [14,20,23]. Let ρ, u_r, u_x and E stand for the density, the radial and axial velocity and the total energy respectively. The pressure function P is given by the perfect gas law depending on ρ and e the specific internal energy:

$$P = (\gamma - 1)\rho e \quad \text{and} \quad E = \rho e + \frac{1}{2}\rho(u_r^2 + u_x^2), \tag{1}$$
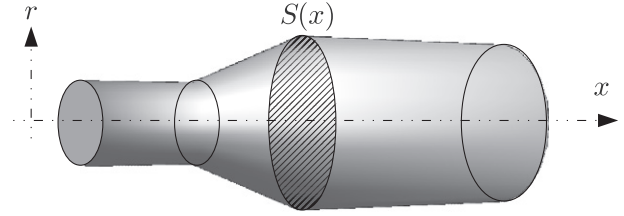

Fig. 1. Compressible fluid flow in axisymmetric geometry: the cross-section $S(x)$ is not constant leading to expansions or compressions of the gas when the section changes.

with γ the ratio of specific heats. The system casts under the generic expression:

$$\frac{\partial(rU)}{\partial t} + \frac{\partial(rF_r(U))}{\partial r} + \frac{\partial(rF_x(U))}{\partial x} = G(U), \tag{2}$$

where $U = (\rho, \rho u_r, \rho u_x, E)$ denotes the conservative variable vector, $F_r(U) = (\rho u_r, \rho u_r^2 + P, \rho u_x u_r, u_r(E + P))$ and $F_x(U) = (\rho u_x, \rho u_r u_x, \rho u_x^2 + P, u_x(E + P))$ are the conservative fluxes and $G(U) = (0, P, 0, 0)$ is the geometric source term deriving from the use of cylindrical coordinates.

In the two last decades, several authors have developed numerical schemes for the Euler system in cylindrical coordinates (see [15,20,24,25] for instance). To address numerical approximation, we employ a second-order finite volume scheme proposed in [14] we shortly sum-up in the present article for the sake of consistency.

To this end, we consider a unstructured mesh $\mathcal{T}_h$ of the two-dimensional domain Ω, constituted of triangles (or cells) $C_i \subset \Omega$, $i = 1, \ldots, I$. We denote by $v(i)$ the index set of the neighbouring triangles C_j which share a common edge S_{ij} with the cell C_i and by $\mathbf{n}_{ij} = (n_{ij,r}, n_{ij,x})$ the outward unit normal vector to C_i (see Fig. 2).

Let $(t^n = n\Delta t)_{n \in \mathbb{N}}$ be a uniform subdivision of the time interval $[0, +\infty)$, U_i^n represents an approximation of the average of U on C_i at time t^n where we have introduced the weighted measures (cell and edge):

$$U_i^n \approx \frac{1}{|C_i|_r} \int_{C_i} U(r, x, t^n) r \, dr \, dx, \quad |C_i|_r = \int_{C_i} r \, dr \, dx, \quad |S_{ij}|_r = \int_{S_{ij}} r \, d\sigma. \tag{3}$$

A general finite volume scheme can be written as:

$$|C_i|_r U_i^{n+1} = |C_i|_r U_i^n - \Delta t \sum_{j \in v(i)} |S_{ij}|_r \mathcal{F}\left(U_i^n, U_j^n, \mathbf{n}_{ij}\right) + \Delta t |C_i| G(U_i^n), \tag{4}$$

where $\mathcal{F}\left(U_i^n, U_j^n, \mathbf{n}_{ij}\right)$ denotes the approximation of the flux across the interface S_{ij} during the time interval $[t^n, t^{n+1}]$, $|C_i|$ the area of cell C_i and $G(U_i^n)$ represents the right-hand side contribution.
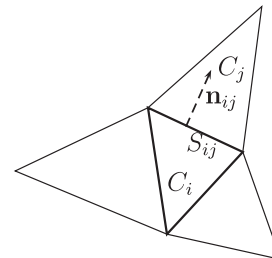

Fig. 2. The two-dimensional mesh: notations. Index set $v(i)$ represents the three neighbouring triangles of cell C_i.

In the present study, we use the Rusanov flux combined with the multislope MUSCL technique on triangles developed in [9,11] to reduce the diffusion effect (see also [14] for a detailed description). An important remark is that the scheme has been designed to respect a crucial well-balanced property: an initial state at rest remains a steady-state at rest.

2.2. Nonconservative Euler system

We now deal with the one-dimensional nonconservative Euler system describing the evolution of a perfect gas in a duct with variable cross-sectional area $S(x)$ following [4]. The system casts in the following nonconservative form:

$$\frac{\partial U}{\partial t} + \frac{\partial F(U)}{\partial x} = G(U)\frac{\partial \phi}{\partial x}, \tag{5}$$

where conservative quantities are represented by vector $U = (\phi\rho, \phi\rho u, \phi E)$ with $\phi(x) = \frac{S(x)}{S_{ref}}$ the ratio between the section area and a reference section, the flux vector by $F(U) = (\phi\rho u, \phi\rho u^2 + \phi P, \phi u(E + P))$ while the nonconservative term writes $G(U) = (0, P, 0)$.

To provide a numerical approximation of the solution of system (5), we first discretize domain $[a, b]$ with uniform cells $C_i = [x_{i-1/2}, x_{i+1/2}]$, $i = 1, \ldots, I - 1$ of length $\Delta x = \frac{b-a}{I}$ where we set $x_{i-1/2} = i\Delta x$ and $x_i = x_{i-1/2} + \frac{\Delta x}{2}$ is the cell center.

Like in the previous subsection, U_i^n is an approximation of the mean value of U on cell C_i at time t^n and we denote by V_i^n the associated vector using the physical variables, $V = (\phi, \rho, u, P)$. We consider a generic well-balanced scheme of the form:

$$U_i^{n+1} = U_i^n - \frac{\Delta t}{\Delta x}\left(F_{i+1/2} + G_{i+1/2}^- - F_{i-1/2} - G_{i-1/2}^+\right), \tag{6}$$

where $F_{i+1/2} = \mathcal{F}(V_i, V_{i+1})$ and $F_{i-1/2} = \mathcal{F}(V_{i-1}, V_i)$ represent the conservative numerical flux across interface $x_{i+1/2}$ and $x_{i-1/2}$ while $G_{i+1/2}^- = \mathcal{G}^-(V_i, V_{i+1})$ and $G_{i-1/2}^+ = \mathcal{G}^+(V_{i-1}, V_i)$ represent the nonconservative contribution across the interface consecutive to the ϕ space variation. To compute the conservative flux, we use the modified version of the Rusanov scheme and design adapted nonconservative flux G^- and G^+ to satisfy the well-balanced property which preserve steady-states solutions (see [13] for a detailed construction of nonconservative schemes).

MUSCL reconstruction method is employed to provide a better accuracy of the numerical approximation and reduce the numerical diffusion. Due to the nonconservative term, one have to pay caution to design the higher-order scheme. We have developed a second-order reconstruction based on the splitting of the ϕ function into a regular part ϕ^r (at least C^1) and a discontinuous piecewise constant one ϕ^d

$$\phi(x) = \phi^d(x) + \phi^r(x),$$

where the regular part is treated as a classical volume source term whereas the discontinuous part is treated with the help of the nonconservative fluxes.

3. Solution configurations for the nonconservative Riemann problem

The finite volume method is based on the solution of a local Riemann problem on every edge of the mesh. Therefore, from a computational point of view, the theoretical analysis of the Riemann problem is of crucial importance. A detailed study in the framework of the nonconservative Euler system has been carried out by Clain and Rochette in [13]. We recall here the main results.

The Riemann problem consists in solving the nonconservative hyperbolic system (5) on $\mathbb{R} \times \mathbb{R}^+$ with the following initial condition: (U_L, ϕ_L), $x < 0$ and (U_R, ϕ_R), $x > 0$.
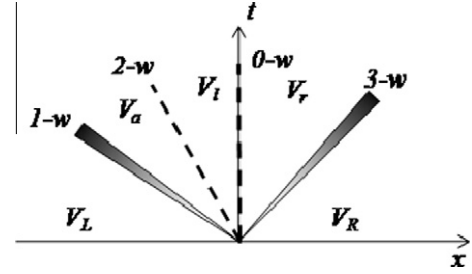

Fig. 3. Example of classical configurations: the B configuration. The genuinely nonlinear simple waves $1 - w$ and $3 - w$ are rarefaction or shock waves whereas the $2 - w$ wave is the $\lambda_2 = u$ contact discontinuity and the $0 - w$ wave is the stationary contact discontinuity wave corresponding to the cross-section discontinuity.

The solution is constituted by a succession of simple waves (rarefaction, shock, contact discontinuity, stationary contact discontinuity) separated by constant states named configuration. The simple waves correspond to a change of state parameterized by the eigenvalues $\lambda_0 = 0$, $\lambda_1 = u - c$, $\lambda_2 = u$, and $\lambda_3 = u + c$. The three last eigenvalues correspond to the classical Euler system while the first eigenvalue λ_0 characterizes the brutal change of cross-section. We recall that the characteristic fields (or simple waves) associated to eigenvalues λ_1 and λ_3 are genuinely nonlinear providing rarefaction (noted $1 - r$ or $3 - r$) or shock (noted $1 - s$ or $3 - s$) while the characteristic fields associated to λ_0 and λ_2 are linearly degenerated (noted $0 - w$ or $2 - w$). We also say that a state $V = (\phi, \rho, u, P)$ is a subsonic, sonic or supersonic state whether we have $u^2 < c^2$, $u^2 = c^2$ or $u^2 > c^2$ where c stands for the sound velocity.

Since the system (5) is not strictly hyperbolic, simple waves can be distinct or superposed inducing a large number of configurations. To select the admissible configuration, we have introduced several criteria: the configuration stability, the sign and the Mach criteria (see [13,21]) leading to the following classification in four groups we shall precise in the next subsections:

1. The classical wave configurations correspond to the situation where the four simple waves are separated by constant states (see Fig. 3).
2. The splitting wave configurations correspond to a situation where a genuinely nonlinear wave is splitted by the $0 - w$ wave (see Fig. 4).
3. The resonance wave configurations correspond to the situation when a genuinely nonlinear wave splits the $0 - w$ wave (see Fig. 5).
4. The resonance and splitting wave configurations are the more complex cases: a genuinely nonlinear wave is splitted by the $0 - w$ wave where one of the part of the wave merges with the $0 - w$ wave (see Fig. 6).
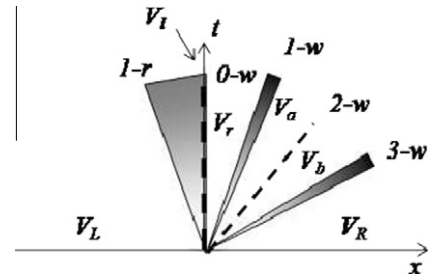

Fig. 4. Example of the splitting configurations: the LR_1 configuration. The $1 - w$ is splitted into two parts, a rarefaction wave on the left side whom the fan reaches the interface and a rarefaction or a shock wave on the right side of the $0 - w$ stationary wave due to the cross-section discontinuity.
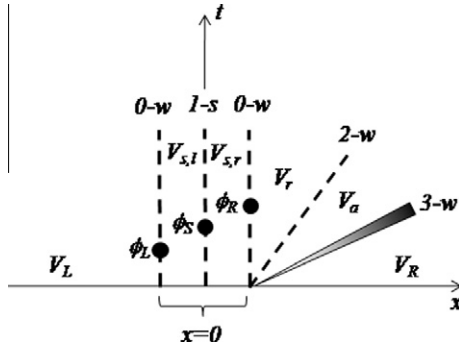
Fig. 5. Example of the resonance configurations: the R_1 configuration. The $1 - s$ is a stationary shock wave superposed to the $0 - w$ wave. From left to right, we have a first $0 - w$ wave transition from ϕ_L to an intermediate value ϕ_s. Then a stationary $1 - s$ shock wave occurs followed by an other $0 - w$ wave transition from ϕ_s to ϕ_R. The two other $2 - w$ and $3 - w$ waves are the classical ones.
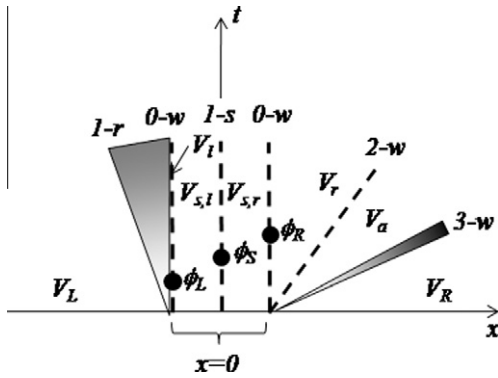

Fig. 6. Example of resonance splitting configurations: LRR_1 configuration. The first part of the $1 - w$ wave is a $1 - r$ rarefaction wave taking place on the left side of the interface and the second part is a $1 - s$ stationary shock superposed to the $0 - w$ stationary for an intermediate value ϕ_s.

3.1. Classical configurations

The classical configurations represent the situations where the eigenvalues λ_k are distinct corresponding to the Riemann problem for the conservative Euler system augmented of the stationary wave located at the interface $x = 0$. We can list four distinct configurations in function of the simple waves position with respect to the interface *i.e.* the $0 - w$ wave. If all the waves are on the left side (configuration A) or on the right side (configuration D) of the interface, we deal with a supersonic flow where all the states are supersonic. The two last configurations correspond to a subsonic flow whether the velocity at the interface is negative (configuration B) or positive (configuration C). As an example, Fig. 3 represents the B configuration where the gas velocity at the interface is negative. Note that the $1 - w$ simple wave is on the left while the $3 - w$ simple wave is on the right.

3.2. Splitting configurations

The configuration where one of the genuinely nonlinear $1 - w$ or $3 - w$ waves is splitted into two waves by the $0 - w$ stationary wave on both side of the interface is a splitting configuration. It is proved that a rarefaction always takes place on the side corresponding to the lower ϕ_L or ϕ_R. Moreover the fan must touch the interface which corresponds to a sonic state. Consequently, there are four distinct configurations in function of the values of ϕ and the genuinely nonlinear waves which are splitted. Configuration LR_1 (Left Rarefaction with the $1 - w$ as shown in Fig. 4) corresponds

to a rarefaction with a $1 - w$ on the left side. Note that the second part of the $1 - w$ is situated on the other side of the interface and can be an other rarefaction or a shock. In a similar way, we use the notations: RR_1 is a Right Rarefaction with the $1 - w$ wave while LR_3 and RR_3 represent the Left Rarefaction and Right Rarefaction for the $3 - w$ wave respectively.

3.3. Resonance wave configurations

We now consider the symmetric case where a genuinely nonlinear $1 - w$ or $3 - w$ wave splits the stationary wave into two parts named the resonance configuration (see [21] p. 892 case 1a (C) for example and [13]). For such a situation, the genuinely nonlinear wave is also a stationary shock corresponding to a subsonic–supersonic transition which takes place at an intermediate value of $\phi_s \in [\phi_L, \phi_R]$. These two situations are referenced by R_1 (see Fig. 5 for instance) or R_3 whether the resonance configuration is obtained with the first or the third eigenvalue.

3.4. Resonance and splitting wave configurations

The last group is the most complicated one since we combine a resonance situation with a splitting situation. A genuinely nonlinear $1 - w$ or $3 - w$ wave is splitted into two pieces where the part situated on the lower cross-section is a rarefaction which touches the interface. The other part is a stationary shock sharing the $0 - w$ wave in another two parts leading to a resonance situation. This configuration has been introduced in [21,12,13]. For example, as shown in Fig. 6, the $1 - w$ is splitted into a rarefaction on the left side of the interface. The first $0 - w$ wave takes place corresponding to a transition from ϕ_L to the intermediate value ϕ_s followed by the second part of the stationary $1 - s$ shock. At last, a second transition with the $0 - w$ occurs from ϕ_s to ϕ_R. The two other waves are the classical ones. The notation LRR_1 means that we deal with a Left Rarefaction and Resonance configuration with the $1 - w$ simple wave while RRR_1 corresponds to the Right Rarefaction and Resonance configuration. In the same way, we have the LRR_3 and the RRR_3 configurations.

4. Comparisons between the two models

The aim of the current section is to draw comparisons between numerical solution of the Riemann problems presented in the previous section of the two models and the exact solution obtained with the inverse Riemann method (see [13]). A similar work has already been carried out by Andrianov and Warnecke [4] using a two-dimensional model to compare the solutions but only for the classical configurations. We propose here a systematic comparison of all the configurations.

For the nonconservative Euler model, we consider a shock tube of length $x = [0:2]$ where the initial discontinuity is located at $x = 0.8$ and we use a subdivision of 1000 mesh cells and an adapted time step to provide the stability. For the axisymmetric model, we consider a cylindrical shock tube of $x = [0:2]$ length and the reference radius is arbitrarily chosen equal to $R_{ref} = 0.15$ corresponding to $\phi = 1$. Like in the previous case, the initial cross-section discontinuity is located at $x = 0.8$. We use a 46,000 triangle cells mesh and the time step is controlled to provide a stable solution. The two models are relied by the duct cross-section ratio with respect to the reference radius and we set :

$$\phi_L = \frac{\pi R_L^2}{\pi R_{ref}^2}, \quad \phi_R = \frac{\pi R_R^2}{\pi R_{ref}^2}, \tag{7}$$

where R_L and R_R are respectively the cross-section duct radius on the left and right side of the interface.

Table 1
Configuration of type $A = \{1 - r, 2 - w, 3 - s, 0 - w\}$.

	ϕ	ρ (kg m^{-3})	u (m s^{-1})	P (Pa)	Mach
V_L	1.0	1.0	−1000	400,000	1.336306
V_a	1.0	0.714825	−757.020985	250,000	1.081867
V_b	1.0	0.5	−757.020985	250,000	0.904813
V_l	1.0	0.177419	−1609.823851	50,000	2.562889
V_R	0.5	0.432066	−1322.085708	173835.409095	1.761576
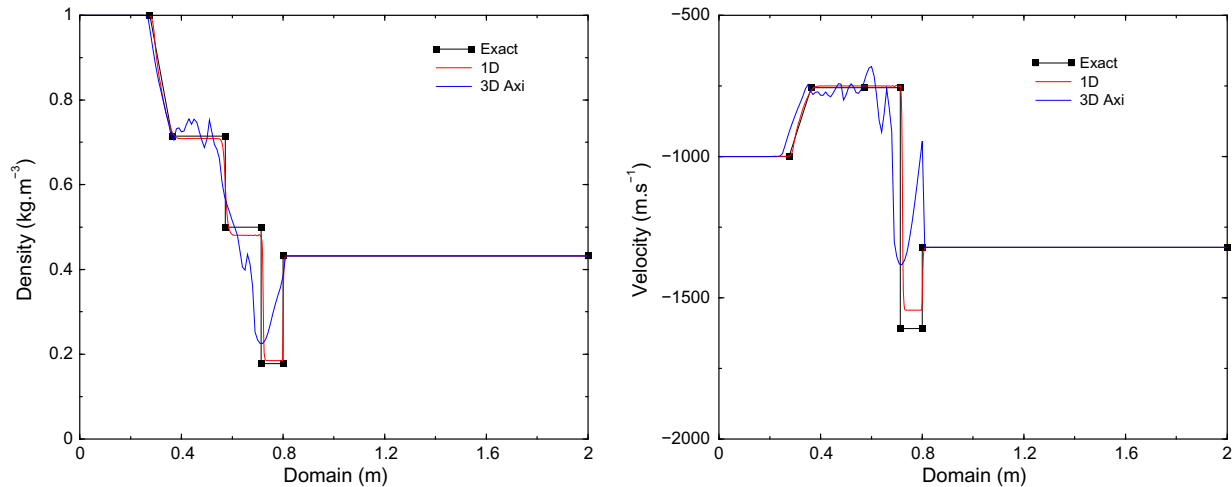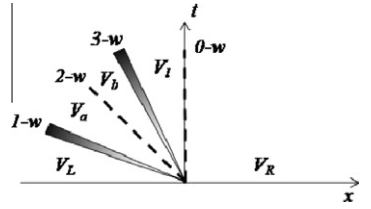
Fig. 7. Configuration of type $A = \{1 - r, 2 - w, 3 - s, 0 - w\}$ at time 3×10^{-4} s.

We now give a detailed comparison of all the configurations. For a given left and right side, we report in the table the exact solutions (note that we can have several solutions) obtained by the inverse Riemann problem where we list the successive constant states from left to right.

Since the reduced model derives from a homogenization procedure, we compare the 1D-nonconservative solution with a homogenized solution provided by the three-dimensional axisymmetric model, for instance a homogenization following the r-direction. To overcome the technical difficulty that the cells are not aligned in the r-direction (we employ an unstructured mesh), we have proceeded in the following way. A very fine uniform grid (r_i, x_j) is applied on the original mesh and we determine the pointwise value $\alpha(r_i, x_j)$ with $\alpha = \rho, u, P, \ldots$ at each node of the grid. Then, we compute the mean value following the r-direction.

Consequently, we print out the density and velocity of the gas for the one-dimensional nonconservative problem at time t_r where the 3D-axisymmetric solution is given by its r-homogenization representation. We also plot a cut of the plane Orx to provide the density map for the axisymmetric problem at the same time t_r.

4.1. Classical wave configurations

4.1.1. Configuration A

Comments. Table 1 gives the exact solution obtained with the inverse Riemann problem while Figs. 7 and 8 show respectively the comparison between the exact solution and the numerical approximations for the density and velocity with the two schemes. We note that the 1D-solutions (exact or numerical) roughly correspond to the axisymmetric case. Indeed, the one-dimensional case corresponds to strict longitudinal waves following the axial direction while the numerical solution of the axisymmetric case provides oblique shocks leading to a more complex density distribution and a smoothing effect for the shocks. However, the axisymmetric numerical solution clearly catches the configuration A in comparison with the exact density solution.

A noticeable difference for the velocity between the two models clearly appears in the vicinity of the change of section. To explain such a discrepancy, we plot the u_x velocity map of the axisymmetric model at the same time in Fig. 9. We observe that the fluid flow develops a vortex in the vicinity of the cross-section discontinuity which generates a counter-current localized in the larger cross-section part ($x < 0.8$). Note that the red[1] zone corresponds to non-negative velocities whereas blue zone represents negative velocities.

The critical point is the position $x = 0.8$. When the homogenization process is performed for $x > 0.8$, we compute a mean velocity very close to the axisymmetric case. Now consider the point $x < 0.8$ very close to 0.8, the homogenization process is performed on two domains: the blue zone provides a negative velocity very close to the one obtained for $x > 0.8$ but the red zone corresponds to a positive velocity. A mean velocity discontinuity results from the change of cross-section and the velocity sign in the "dead zone". The crucial point is that the 1D model does not take into account the recirculating flow and the two numerical solutions do not correspond at that location. Nevertheless, the $1 - r$ simple wave position of the velocity is well-determined which means that the 1D model is still pertinent.

---

[1] For interpretation of colour in Figs. 7–52 and 54–57, the reader is referred to the web version of this article.
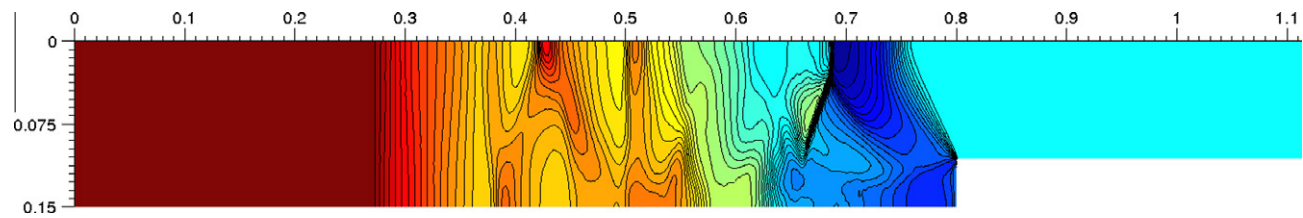
Fig. 8. Fifty isodensity from 1 to 0.09 at time 3×10^{-4} s.
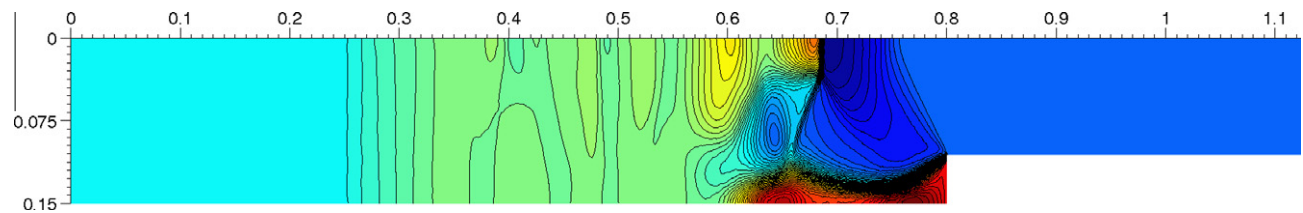

Fig. 9. Fifty isovalue of u_x from -1750 to 265 at time 3×10^{-4} s.

4.1.2. Configuration B

Comments. Table 2 gives the exact solution obtained with the inverse Riemann problem while Figs. 10 and 11 show respectively the comparison between the exact solution and the numerical approximations for the density and velocity with the two schemes. For this configuration, we observe that the 1D-solutions (exact or numerical) perfectly fit with the axisymmetric solution since the shock waves are principally longitudinal reducing the smoothing effect.

4.1.3. Configuration C

Comments. Table 3 gives the exact solution obtained with the inverse Riemann problem while Figs. 12 and 13 show respectively the comparison between the exact solution and the numerical approximations for the density and velocity with the two schemes. In the vicinity of the cross-section discontinuity, we note differences between the solutions of the axisymmetric problem and the nonconservative one. The very small jump of cross-section seems to be smoothed in the three-dimensional context while

Table 2
Configuration of type $B = \{1 - r, 2 - w, 0 - w, 3 - s\}$.

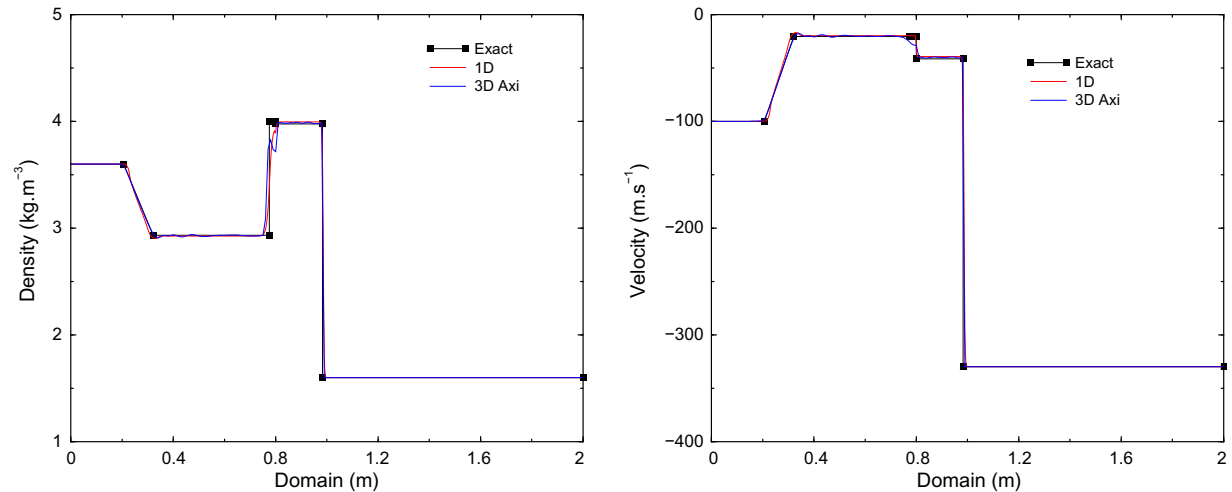|	ϕ	ρ (kg m^{-3})	u (m s^{-1})	P (Pa)	Mach
V_L	1.0	3.6	-100	400,000	0.253546
V_a	1.0	2.931302	-20.597552	300,000	0.054415
V_l	1.0	4.0	-20.597552	300,000	0.063565
V_r	0.5	3.975401	-41.450012	297420.273072	0.128075
V_R	0.5	1.597881	-329.977019	75,000	1.287245

Fig. 10. Configuration of type $B = \{1 - r, 2 - w, 0 - w, 3 - s\}$ at time 12×10^{-4} s.
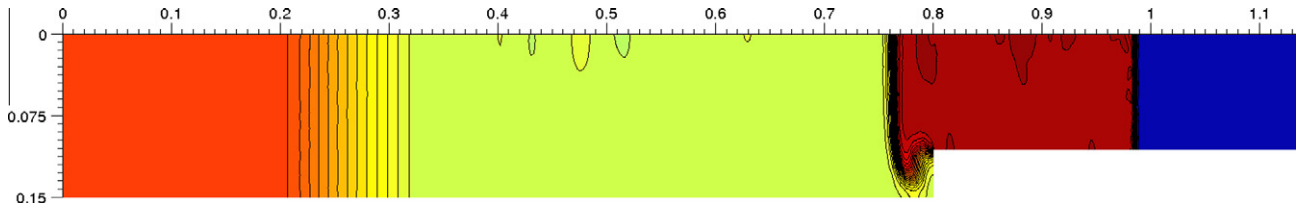
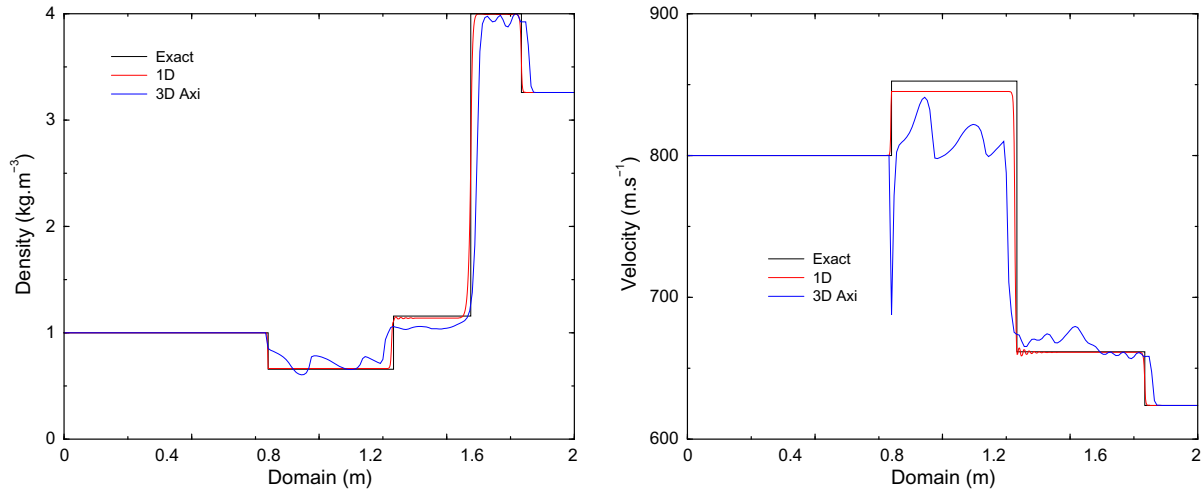**Fig. 11.** Fifty isodensity from 1.5 to 4 at time 12×10^{-4} s.

Table 3
Configuration of type $C = \{1 - r, 0 - w, 2 - w, 3 - s\}$.

	ϕ	ρ (kg m^{-3})	u (m s^{-1})	P (Pa)	Mach	
V_L	0.9	3.6	100	300,000	0.292770	
V_l	0.9	2.694778	196.112884	200,000	0.608399	
V_r	1.0	2.828882	168.134511	214071.314011	0.516560	
V_a	1.0	3.4	168.134511	214071.314011	0.566308	
V_R	1.0	3.238852	153.784754	200,000	0.523034	
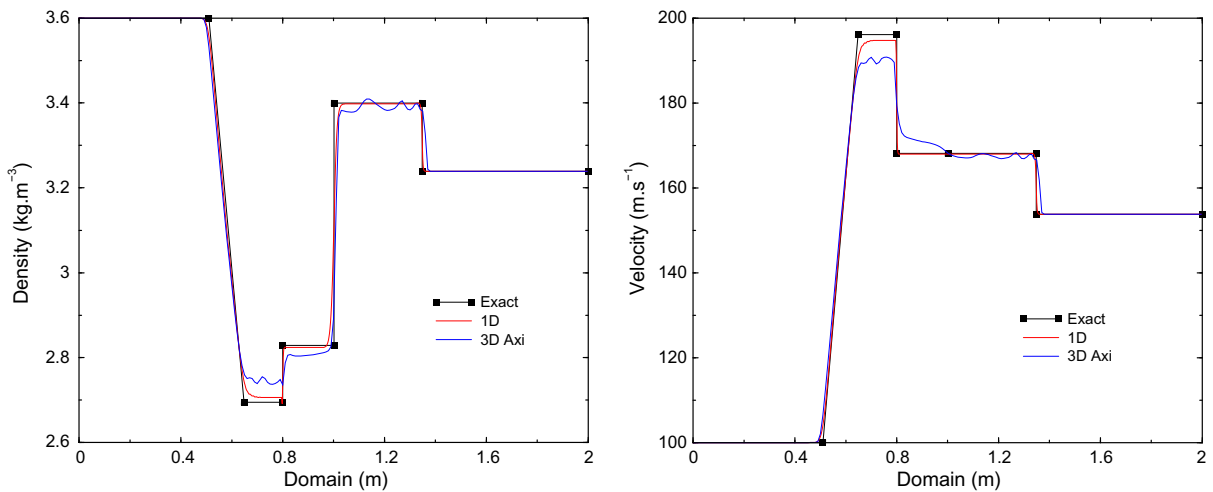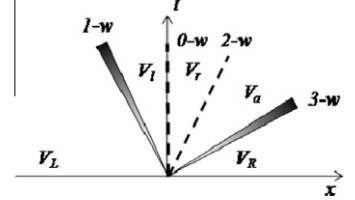
Fig. 12. Configuration of type $C = \{1 - r, 0 - w, 2 - w, 3 - s\}$ at time 12×10^{-4} s.
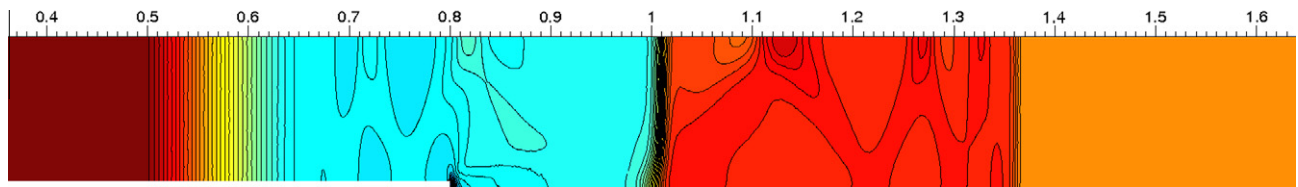
Fig. 13. Fifty isodensity from 2.3 to 3.6 at time 12×10^{-4} s.

the one-dimensional model preserves the stationary shock. However, the other waves fit well with the exact solution.
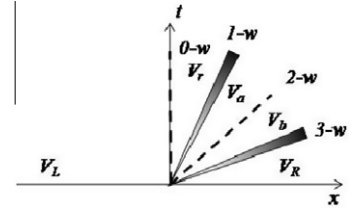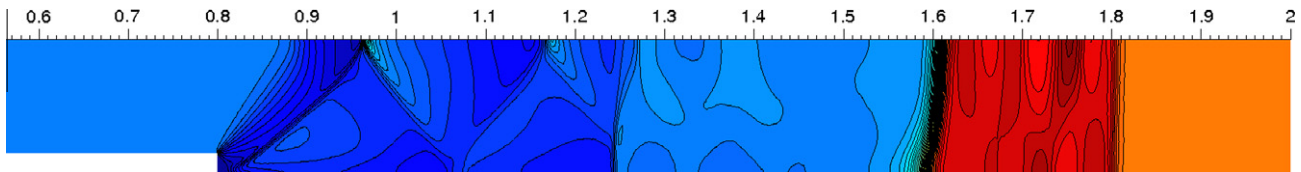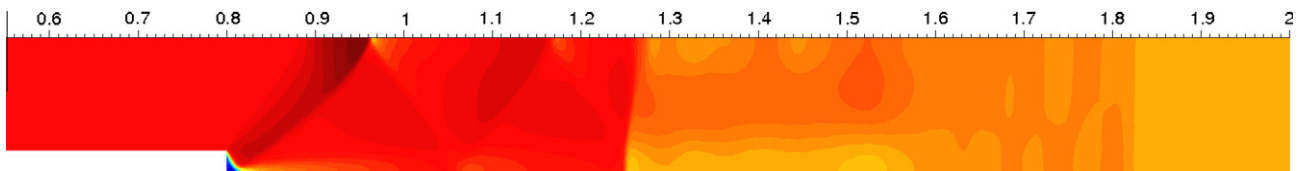
4.1.4. Configuration D

Comments. Table 4 gives the exact solution obtained with the inverse Riemann problem while Figs. 14 and 15 show respectively the comparison between the exact solution and the numerical approximations for the density and velocity with the two schemes. The profiles are roughly respected in the shock tube but we note

important oscillations of the axisymmetric solution (essentially on the first left plateau).

Like configuration A, we plot the u_x velocity map in Fig. 16 to observe slanted waves stemming from the three-dimensional context (radial waves are generated at the interface) and a recirculating flow (counter-current) with a "dead zone". The remarks are similar to the ones exposed in case A. A small vortex generates local negative velocities in the corner leading to a discontinuity of the mean velocity. Such a phenomena is not taken into account in the homogenized one-dimensional model.

Table 4
Configuration of type $D = \{0 - w, 1 - s, 2 - w, 3 - s\}$.

	ϕ	ρ (kg m^{-3})	u (m s^{-1})	P (Pa)	Mach
V_L	0.7	1.0	800	80,000	2.390457
V_r	1.0	0.656948	852.426066	44425.652469	2.770393
V_a	1.0	1.154958	661.437525	100,000	1.899800
V_b	1.0	4.0	661.437525	100,000	3.535532
V_R	1.0	3.259259	623.748607	75,000	3.475157

Fig. 14. Configuration of type $D = \{0 - w, 1 - s, 2 - w, 3 - s\}$ at time 12×10^{-4} s.

Fig. 15. Fifty isodensity from 0.06 to 4.3 at time 12×10^{-4} s.

Fig. 16. Fifty isovalue of u_x from -165 to 950 at time 12×10^{-4} s.

4.2. Splitting wave configurations

4.2.1. Configuration LR_1 with rarefaction

Comments. Table 5 gives the exact solution obtained with the inverse Riemann problem while Figs. 17 and 18 show respectively the comparison between the exact solution and the numerical approximations for the density and velocity with the two schemes. We first remark that both the 1D-model and the 3D-model present left rarefaction which spreads out from the left subsonic state so far to a sonic state at the interface as stated by the theory in [13]. The curves fit well despite some oscillations of the V_r state for the three-dimensional configuration consecutive to oblique

shocks. Thanks to our experience and after a lot of numerical experiments, it appears that this particular state (just before or just after a rarefaction reaching the sonic point) is always difficult to accurately approximate. It is one of the most sensitive state.
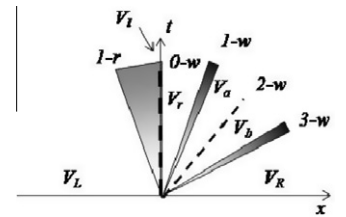
4.2.2. Configuration LR_1 with shock

Comments. Table 6 gives the exact solution obtained with the inverse Riemann problem while Figs. 19 and 20 show respectively the comparison between the exact solution and the numerical approximations for the density and velocity with the two schemes. The previous comments apply to this configuration: the intermediate state V_r for the 3D-solution presents strong oscillations and we

Table 5
Configuration of type LR_1 with rarefaction $LR_1\_rar = \{1 - r, 0 - w, 1 - r, 2 - w, 3 - r\}$.

	ϕ	ρ (kg m^{-3})	u (m s^{-1})	P (Pa)	Mach
V_L	0.8	5.0	250	400,000	0.747018
V_l	0.8	4.031127	320.553342	295868.736587	1.0
V_r	1.0	2.262737	456.859511	131822.563570	1.599708
V_a	1.0	1.583820	555.189919	80,000	2.087783
V_b	1.0	1.68	555.189919	80,000	2.150241
V_R	1.0	2.376396	647.909308	130,000	2.341197
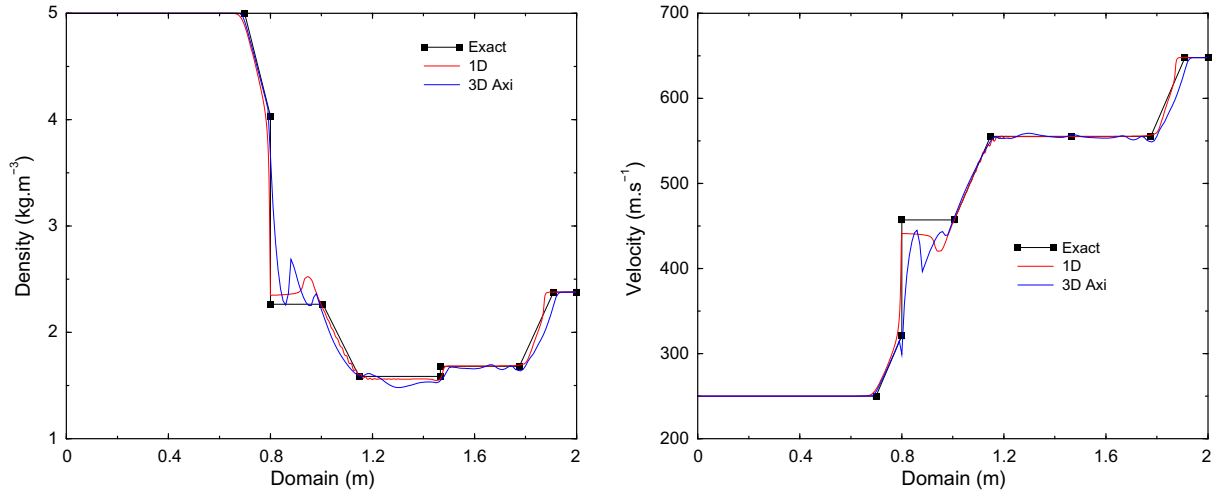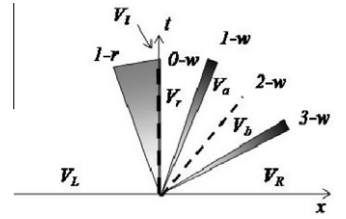
Fig. 17. Configuration of type $LR_1\_rar = \{1 - r, 0 - w, 1 - r, 2 - w, 3 - r\}$ at time 12×10^{-4} s.
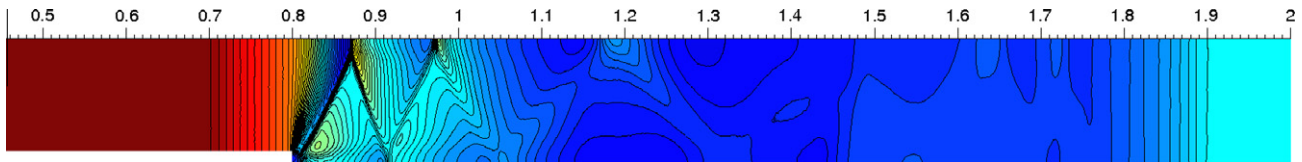
Fig. 18. Fifty isodensity from 1 to 5 at time 12×10^{-4} s.

Table 6
Configuration of type LR_1 with shock $LR_1\_sck = \{1 - r, 0 - w, 1 - s, 2 - w, 3 - s\}$.

	ϕ	ρ (kg m^{-3})	u (m s^{-1})	P (Pa)	Mach
V_L	0.8	5.0	200	300,000	0.690066
V_l	0.8	3.835307	274.856279	206958.559906	1.0
V_r	1.0	2.152820	391.731075	92209.160840	1.599708
V_a	1.0	3.037373	303.313516	150,000	1.153536
V_b	1.0	1.68	303.313516	150,000	0.857900
V_R	1.0	1.033846	136.275239	75,000	0.427612

observe that the $1 - s$ shock computed with the 1D-model parting the V_r and V_a states is smoothed. However, the axisymmetric solution clearly coincides well with the one-dimensional solution.

4.2.3. Configuration LR_3 with rarefaction

Comments. Table 7 gives the exact solution obtained with the inverse Riemann problem while Figs. 21 and 22 show respectively the comparison between the exact solution and the numerical

approximations for the density and velocity with the two schemes. The theoretical small $3 - r$ rarefaction which takes place from state V_b to the sonic point V_l predicted by the one-dimensional model is not well reproduced by the three-dimensional model. One more time, small oscillations consecutive to oblique waves before and after the cross-section change appear. Nevertheless, the intermediate states correspond and the two simulations provide a LR_3 configuration.
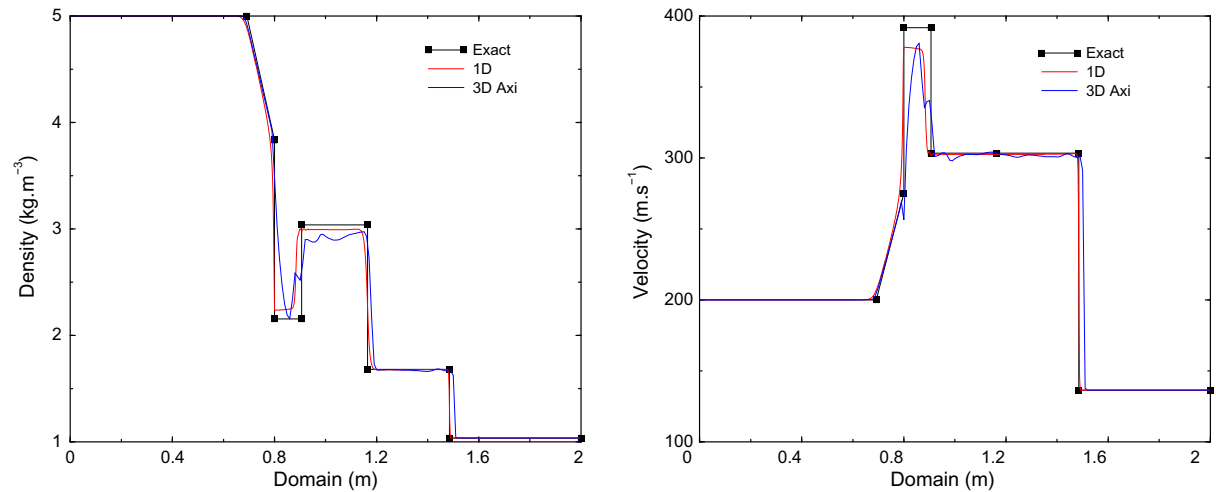
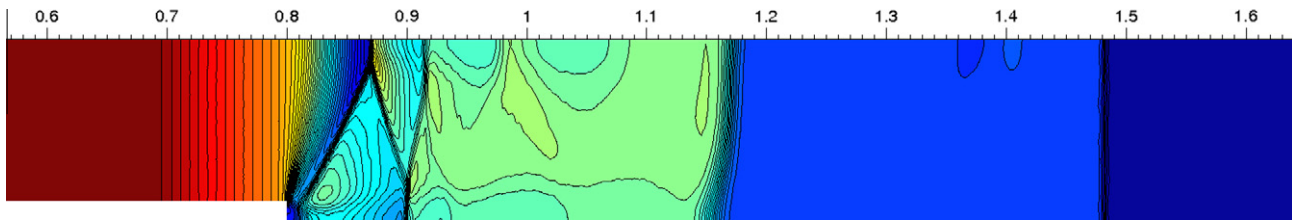**Fig. 19.** Configuration of type LR_1_sck = $\{1-r, 0-w, 1-s, 2-w, 3-s\}$ at time 12×10^{-4} s.

Fig. 20. Fifty isodensity from 1 to 5 at time 12×10^{-4} s.

Table 7
Configuration of type LR_3 with rarefaction LR_3_rar = $\{1-s, 2-w, 3-r, 0-w, 3-r\}$.

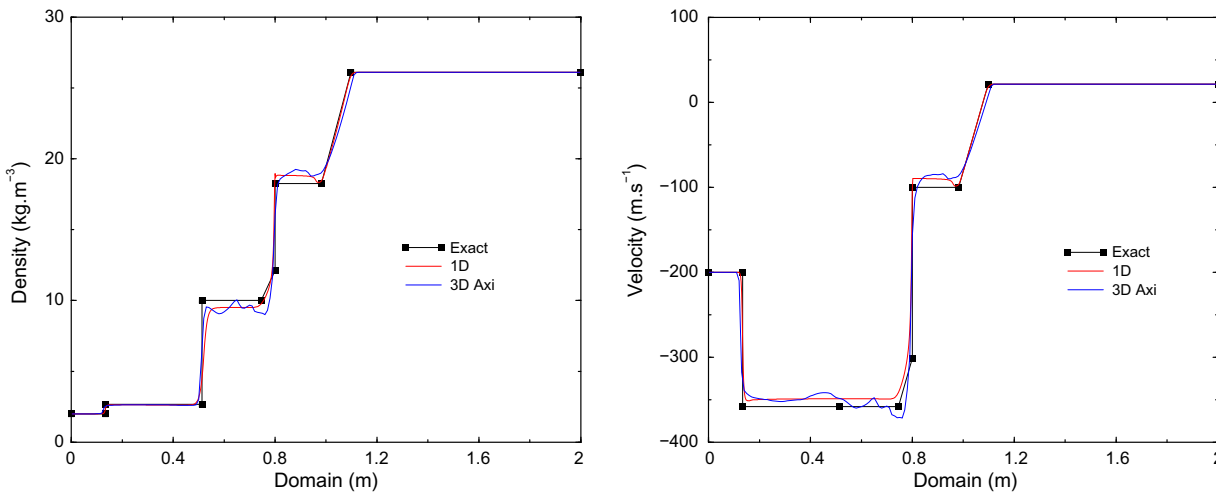|	ϕ	ρ (kg m^{-3})	u (m s^{-1})	P (Pa)	Mach
V_L	0.5	2.0	−200	400,000	0.377964
V_a	0.5	2.666667	−358.113883	600,000	0.638066
V_b	0.5	10.0	−358.113883	600,000	1.235610
V_l	0.5	12.123795	−301.208593	785679.190499	1.0
V_r	1.0	18.258264	−100.003790	1393780.920329	0.305904
V_R	1.0	26.112017	21.244529	2300000.0	0.060498

Fig. 21. Configuration of type LR_3_rar = $\{1-s, 2-w, 3-r, 0-w, 3-r\}$ at time 8×10^{-4} s.
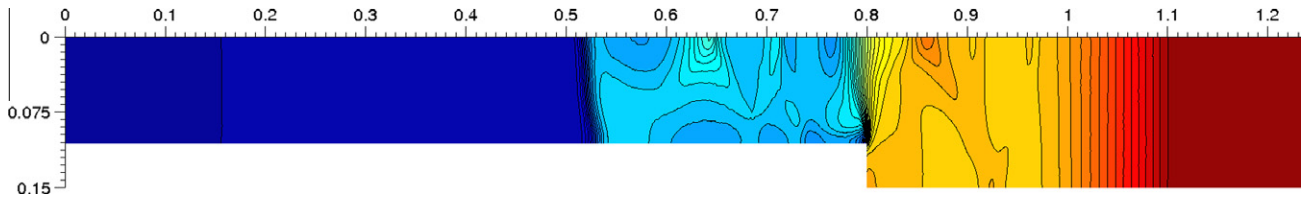
Fig. 22. Fifty isodensity from 2 to 27 at time 8×10^{-4} s.

4.2.4. Configuration LR_3 with shock

Comments. Table 8 gives the exact solution obtained with the inverse Riemann problem while Figs. 23 and 24 show respectively the comparison between the exact solution and the numerical approximations for the density and velocity with the two schemes. The present simulation is very similar to the former one but we have, in this case, a $3 - s$ shock to link V_r to V_R on the right side of the interface while we have a $3 - r$ rarefaction to link the states in the previous case. Comments and remarks are very similar, the

two simulations provide the same configuration but oscillations due to oblique shocks appear with the three-dimensional model.

4.2.5. Configuration RR_1 with rarefaction

Comments. Table 9 gives the exact solution obtained with the inverse Riemann problem while Figs. 25 and 26 show respectively the comparison between the exact solution and the numerical approximations for the density and velocity with the two schemes. We now consider situations when the lowest cross-section is on

Table 8
Configuration of type LR_3 with shock $LR_3\_sck = \{1 - s, 2 - w, 3 - r, 0 - w, 3 - s\}$.

	ϕ	ρ (kg m^{-3})	u (m s^{-1})	P (Pa)	Mach
V_L	0.5	5.0	−250	400,000	0.747018
V_a	0.5	6.666667	−350	600,000	0.986013
V_b	0.5	10.0	−350	600,000	1.207615
V_l	0.5	11.854071	−299.856279	761317.446137	1.0
V_r	1.0	17.852064	−99.554810	1350563.618802	0.305904
V_R	1.0	4.619603	−542.096262	130000.0	2.731134
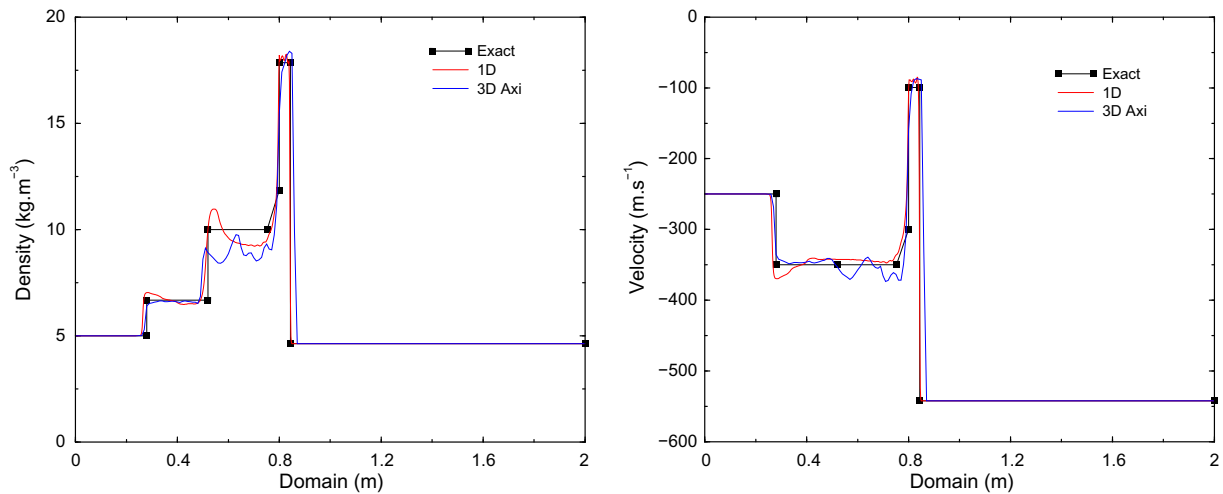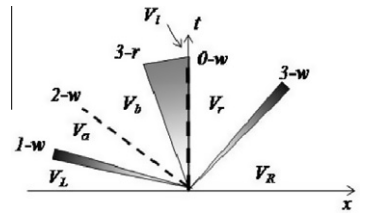
Fig. 23. Configuration of type $LR_3\_sck = \{1 - s, 2 - w, 3 - r, 0 - w, 3 - s\}$ at time 8×10^{-4} s.
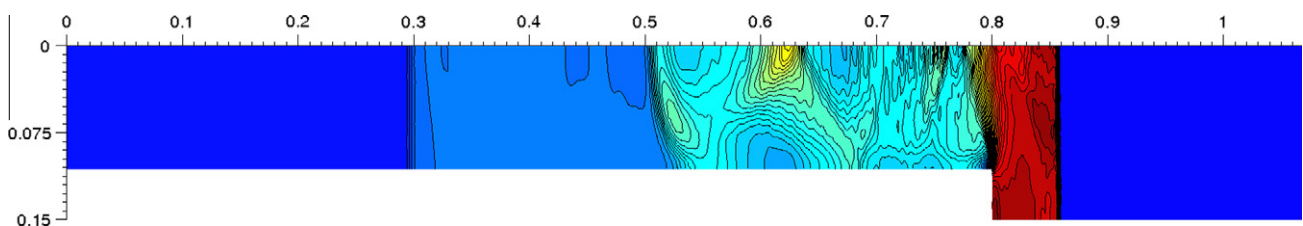

Fig. 24. Fifty isodensity from 3 to 19 at time 8×10^{-4} s.

Table 9

Configuration of type RR_1 with rarefaction $RR_1\_rar = \{1 - r, 0 - w, 1 - r, 2 - w, 3 - s\}$.

	ϕ	ρ (kg m^{-3})	u (m s^{-1})	P (Pa)	Mach
V_L	1.0	3.6	0.0	400,000	0.0
V_I	1.0	2.501047	138.544575	240218.917576	0.377818
V_r	0.6	1.701108	339.491071	140042.899031	0.999999
V_a	0.6	1.337395	419.224375	100,000	1.295723
V_b	0.6	0.7	419.224375	100,000	0.937414
V_R	0.6	0.570370	329.130629	75,000	0.767100
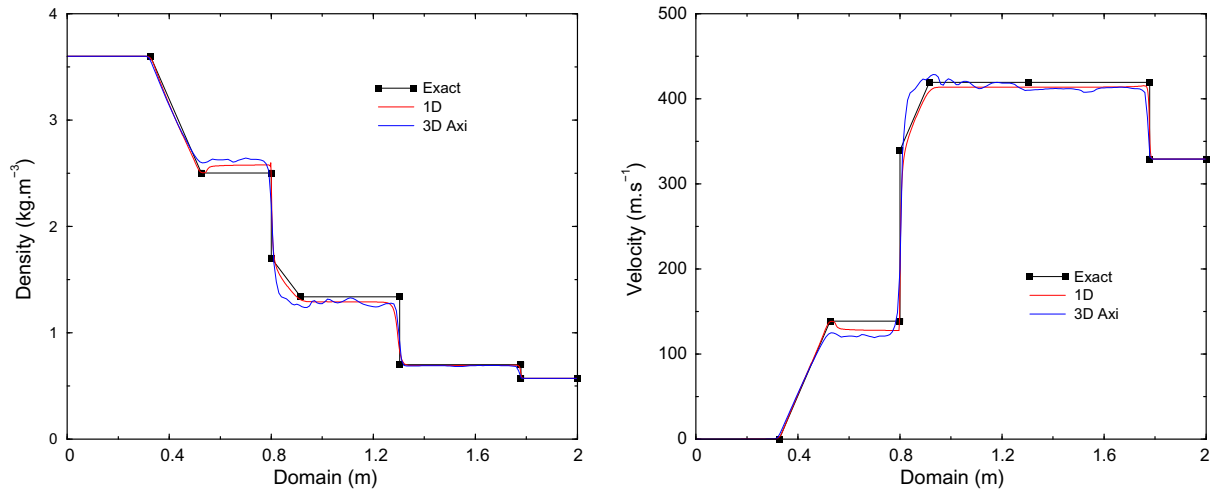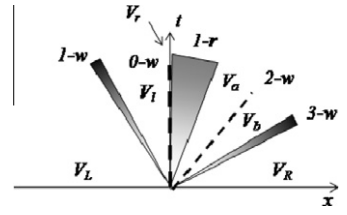
Fig. 25. Configuration of type $RR_1\_rar = \{1 - r, 0 - w, 1 - r, 2 - w, 3 - s\}$ at time 12×10^{-4} s.
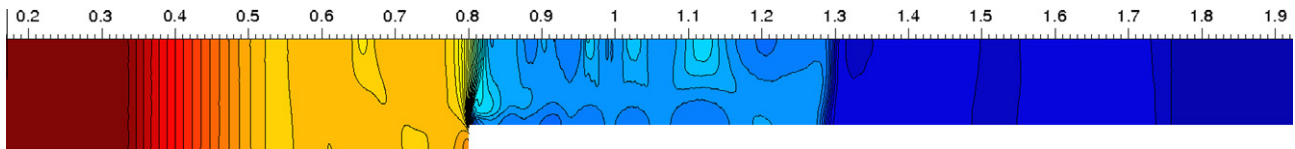
Fig. 26. Fifty isodensity from 0.5 to 3.6 at time 12×10^{-4} s.

the right side leading this time to a right rarefaction. We observe that for this particular configuration the three curves suit well.

4.2.6. Configuration RR_1 with shock

Comments. Table 10 gives the exact solution obtained with the inverse Riemann problem while Figs. 27 and 28 show respectively the comparison between the exact solution and the numerical approximations for the density and velocity with the two schemes. In contrast with the previous case, the second part of the $1 - w$

wave which shares the states V_L and V_I is a shock (a rarefaction in the former case). Note that despite the large cross-section ratio, we obtain the same configuration between the "real" three-dimensional model and the "homogenized" one-dimensional model.

4.2.7. Configuration RR_3 with rarefaction

Comments. Table 11 gives the exact solution obtained with the inverse Riemann problem while Figs. 29 and 30 show respectively the comparison between the exact solution and the numerical

Table 10

Configuration of type RR_1 with shock $RR_1\_sck = \{1 - s, 0 - w, 1 - r, 2 - w, 3 - s\}$.

	ϕ	ρ (kg m^{-3})	u (m s^{-1})	P (Pa)	Mach
V_L	1.0	3.0	100	200,000	0.327327
V_I	1.0	3.259671	74.409093	224662.868292	0.239543
V_r	0.4	2.126227	285.187189	123521.258857	1.0
V_a	0.4	1.559044	370.984366	80000.0	1.384127
V_b	0.4	1.0	370.984366	80000.0	1.108528
V_R	0.4	0.862385	322.059761	65000.0	0.991440
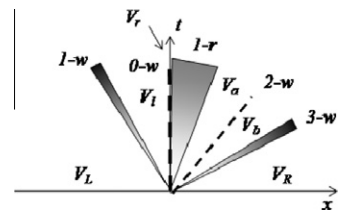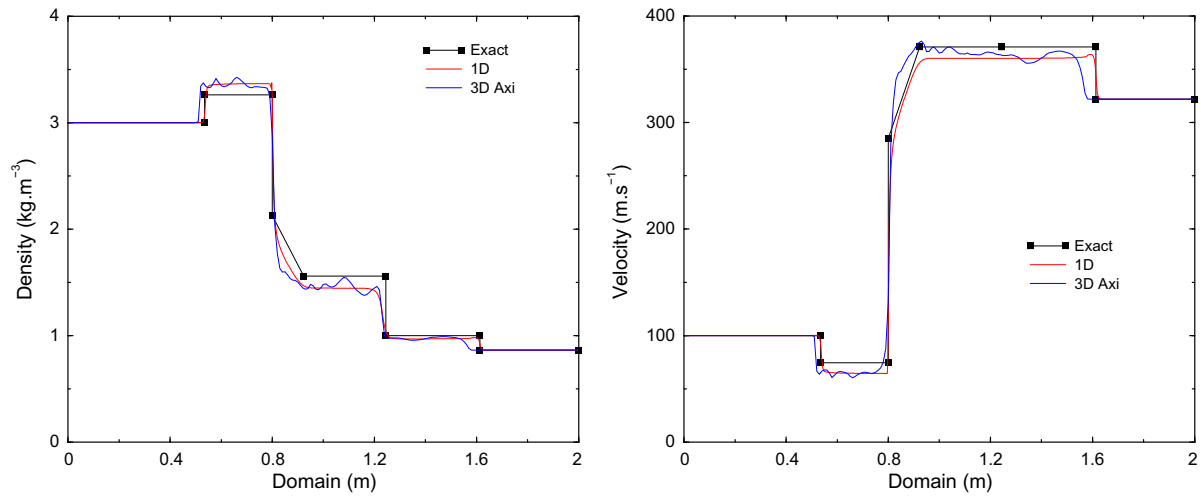
Fig. 27. Configuration of type $RR_1\_sck = \{1 - s, 0 - w, 1 - r, 2 - w, 3 - s\}$ at time 12×10^{-4} s.
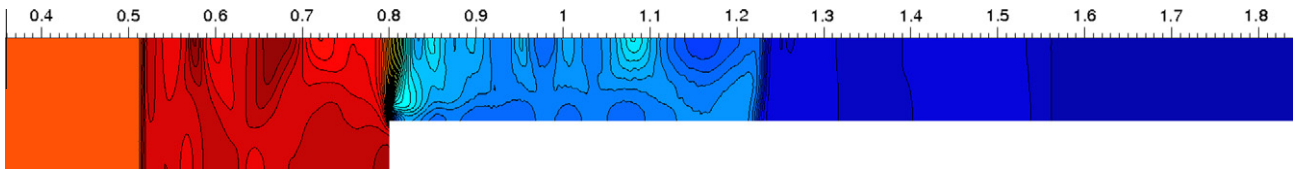

Fig. 28. Fifty isodensity from 0.8 to 3.6 at time 12×10^{-4} s.

Table 11
Configuration of type RR_3 with rarefaction $RR_3\_rar = \{1 - s, 2 - w, 3 - r, 0 - w, 3 - r\}$.

	ϕ	ρ (kg m^{-3})	u (m s^{-1})	P (Pa)	Mach	
V_L	1.0	5.0	−250	100,000	1.494036	
V_a	1.0	6.666667	−300	150,000	1.690309	
V_b	1.0	8.0	−300	150,000	1.851640	
V_l	1.0	9.648037	−269.076202	194975.414173	1.599708	
V_r	0.8	17.188238	−188.796060	437611.952725	1.0	
V_R	0.8	22.801474	−133.905733	650,000	0.670286	
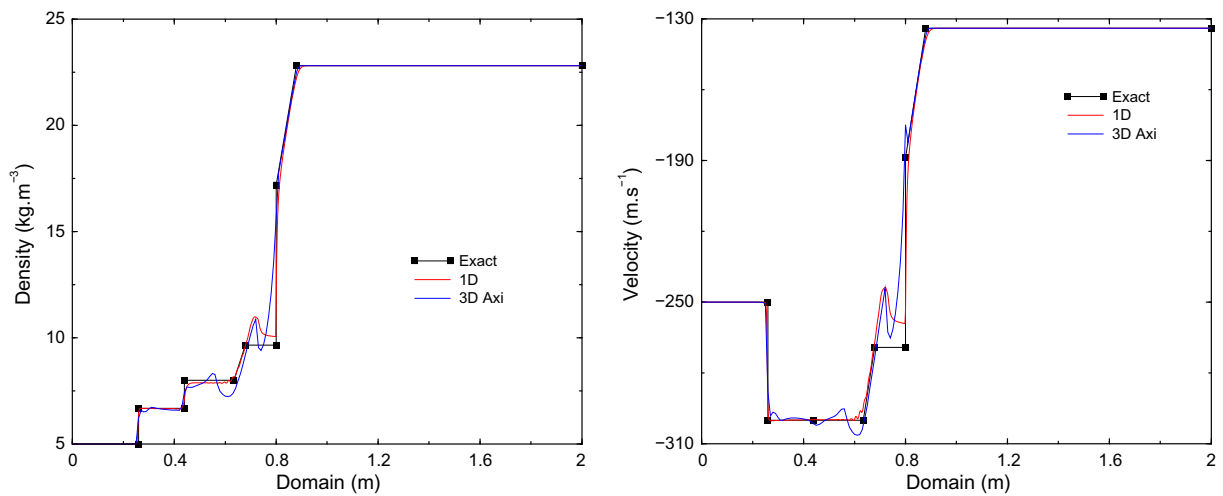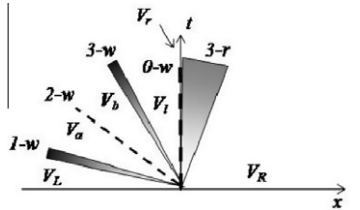
Fig. 29. Configuration of type $RR_3\_rar = \{1 - s, 2 - w, 3 - r, 0 - w, 3 - r\}$ at time 12×10^{-4} s.
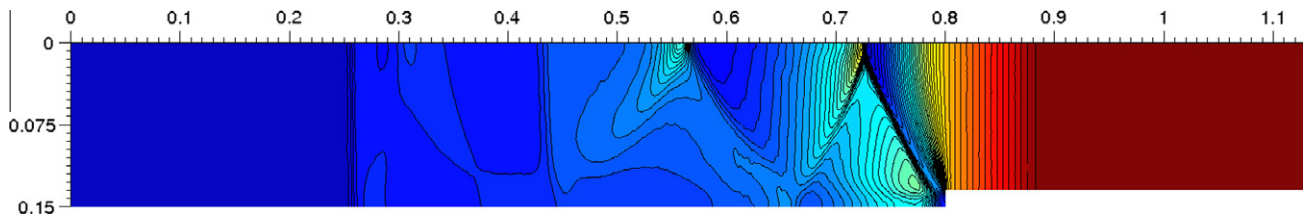
Fig. 30. Fifty isodensity from 4 to 23 at time 12×10^{-4} s.

approximations for the density and velocity with the two schemes. The present simulation shows clearly the oscillations origin. Strong slanted shocks propagate and the nice plateau (constant solution) obtained with the one-dimensional is poorly reproduced by the axisymmetric solution. Nevertheless, the theoretical configuration predicted by the 1D-model is confirmed by the 3D-simulation which indicates the adequacy of the homogenized model with the "real" one.

4.2.8. Configuration RR_3 with shock

Comments. Table 12 gives the exact solution obtained with the inverse Riemann problem while Figs. 31 and 32 show respectively the comparison between the exact solution and the numerical approximations for the density and velocity with the two schemes. With this last configuration of the RR group, we observe that the density curve of the 3D-solution fits rather well with the theoretical density curve but the velocity are very poorly approximated. The origin of such a difference seems to be the contact discontinuity which is clearly not preserved by the axisymmetric

solution. In this case, it becomes difficult to draw comparisons between the two models although the configurations are really similar.

4.3. Resonance wave configurations

4.3.1. Configuration R_1

Comments. Table 13 gives the exact solution obtained with the inverse Riemann problem while Figs. 33 and 34 show respectively the comparison between the exact solution and the numerical approximations for the density and velocity with the two schemes. In the resonance configuration, the transition between the state V_L and V_r requires two intermediate states $V_{s,l}$ and $V_{s,r}$ which are superposed with the interface with two different densities (indicated by the black box in Fig. 33). We indeed observe that the three-dimensional simulation presents a peak at the interface which corresponds to the higher intermediate density. It is remarkable to see that the 1D-exact solution coincides very well with the axisymmetric solution.

Table 12
Configuration of type RR_3 with shock $RR_3\_sck = \{1 - s, 2 - w, 3 - s, 0 - w, 3 - r\}$.

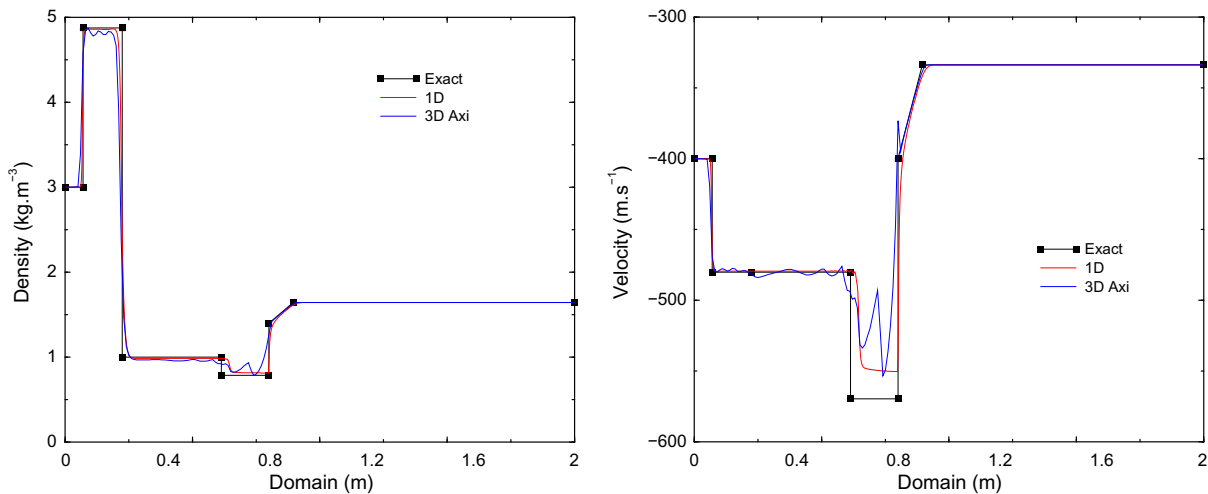|	ϕ	ρ (kg m^{-3})	u (m s^{-1})	P (Pa)	Mach	
V_L	1.0	3.0	−400	50,000	2.618615	
V_a	1.0	4.875	−480.064077	100000.0	2.832843	
V_b	1.0	1.0	−480.064077	100000.0	1.283025	
V_l	1.0	0.783632	−569.600910	70964.939235	1.599708	
V_r	0.8	1.396062	−399.657818	159277.033801	1.0	
V_R	0.8	1.642596	−333.595729	200000.0	0.807992	

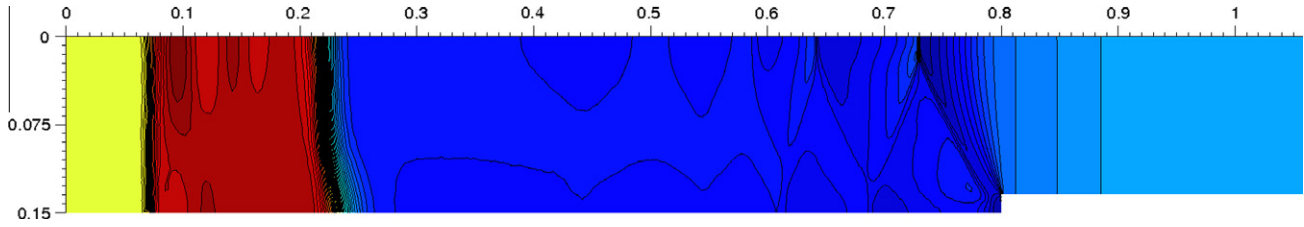**Fig. 31.** Configuration of type $RR_3\_sck = \{1 - s, 2 - w, 3 - s, 0 - w, 3 - r\}$ at time 12×10^{-4} s.
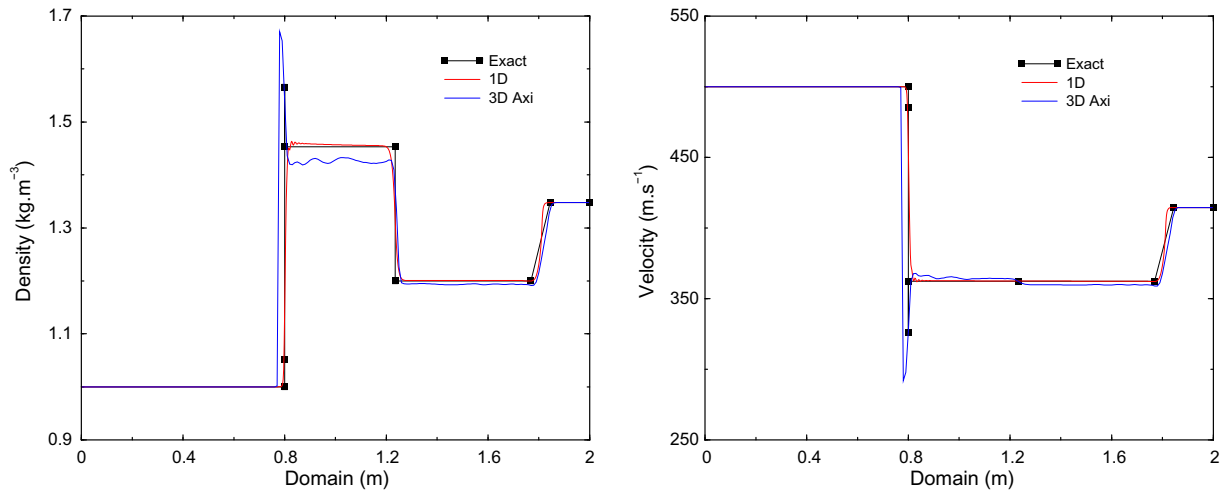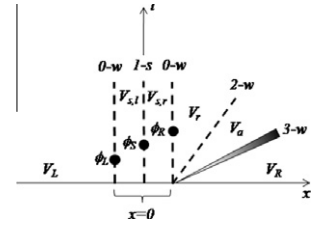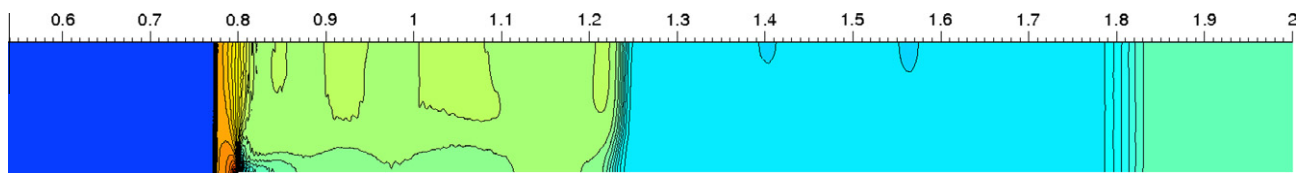
Fig. 32. Fifty isodensity from 0.4 to 5 at time 12×10^{-4} s.

Table 13
Configuration of type $R_1 = \{0 - w, 1 - s, 0 - w, 2 - w, 3 - r\}$.

	ϕ	ρ (kg m^{-3})	u (m s^{-1})	P (Pa)	Mach
V_L	1.0	1.0	500	100,000	1.336306
$V_{s,l}$	0.979139	1.051791	485.507722	107325.116343	1.284536
$V_{s,r}$	0.979139	1.565848	326.119084	188717.365256	0.793928
V_r	0.95	1.453274	362.158786	170000.000005	0.894920
V_a	0.95	1.2	362.158786	170000.000005	0.813207
V_R	0.95	1.347710	414.461597	200000.0	0.909292

Fig. 33. Configuration of type $R_1 = \{0 - w, 1 - s, 0 - w, 2 - w, 3 - r\}$ at time 12×10^{-4} s.

Fig. 34. Fifty isodensity from 0.8 to 2 at time 12×10^{-4} s.

4.3.2. Configuration R_3

Comments. Table 14 gives the exact solution obtained with the inverse Riemann problem while Figs. 35 and 36 show respectively the comparison between the exact solution and the numerical approximations for the density and velocity with the two schemes. We now consider a similar resonance situation but with the $3 - s$ stationary shock inside the interface. The three solutions fit nicely and no peak is observed since the intermediate state density $V_{s,l}$, $V_{s,r}$ belongs to the interval $[V_R, V_l]$. This point seems to confirm that the peak in the previous 3D approximation is not a numerical artefact but an approximation of the intermediate state densities.

4.4. Resonance and splitting wave configurations

4.4.1. Configuration LRR_1

Comments. Table 15 gives the exact solution obtained with the inverse Riemann problem while Figs. 37 and 38 show respectively the comparison between the exact solution and the numerical approximations for the density and velocity with the two schemes. We here deal with the more complex situation where we have both a splitting wave and a resonance situation. The positive point is that we obtain the same theoretical configuration both with the one-dimensional and the three-dimensional model which suggests

Table 14
Configuration of type $R_3 = \{1 - r, 2 - w, 0 - w, 3 - s, 0 - w\}$.

	ϕ	ρ (kg m^{-3})	u (m s^{-1})	P (Pa)	Mach	
V_L	0.9	1.0	−1000	400,000	1.336306	
V_a	0.9	0.909028	−929.300937	350,000	1.265747	
V_l	0.9	0.3	−929.300937	350,000	0.727142	
$V_{s,l}$	0.947867	0.314418	−841.908993	373773.744392	0.652605	
$V_{s,r}$	0.947867	0.148077	−1787.656974	23423.468739	1.654876	
V_R	1.0	0.136386	−1839.710883	110000.000014	1.731309	
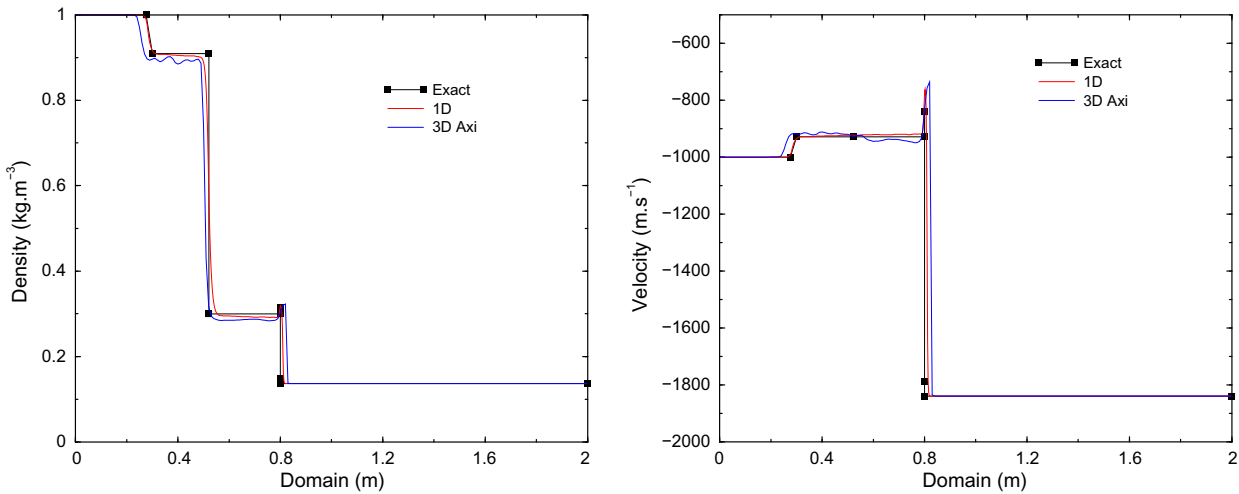
Fig. 35. Configuration of type $R_3 = \{1 - r, 2 - w, 0 - w, 3 - s, 0 - w\}$ at time 3×10^{-4} s.
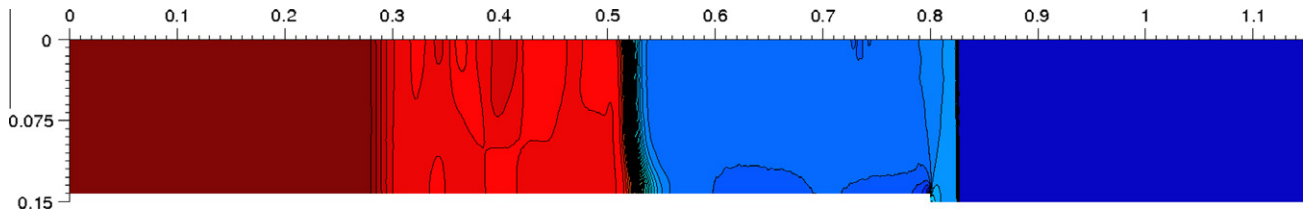
Fig. 36. Fifty isodensity from 0.1 to 1 at time 3×10^{-4} s.

Table 15
Configuration of type $LRR_1 = \{1 - r, 0 - w, 1 - s, 0 - w, 2 - w, 3 - s\}$.

	ϕ	ρ	u	P	Mach	
V_L	1.3	1.862000	0.826000	2.458300	0.607559	
V_l	1.3	1.327678	1.270616	1.531063	1.0	
$V_{s,l}$	1.31102	1.214478	1.377370	1.351478	1.103511	
$V_{s,r}$	1.31102	1.427126	1.172136	1.694791	0.909049	
V_r	1.6	1.789307	0.766029	2.326095	0.567819	
V_a	1.6	2.0	0.766029	2.326095	0.600320	
V_R	1.6	1.795636	0.629806	2.0	0.504356	

that such a configuration is physical. The negative point is the very poor approximation of the $1 - r$ rarefaction on the left side of the interface that reaches the sonic point. We have performed numerical simulations with finer meshes with the axisymmetric model to see if, possibly, we better catch the rarefaction but the tests were negative.
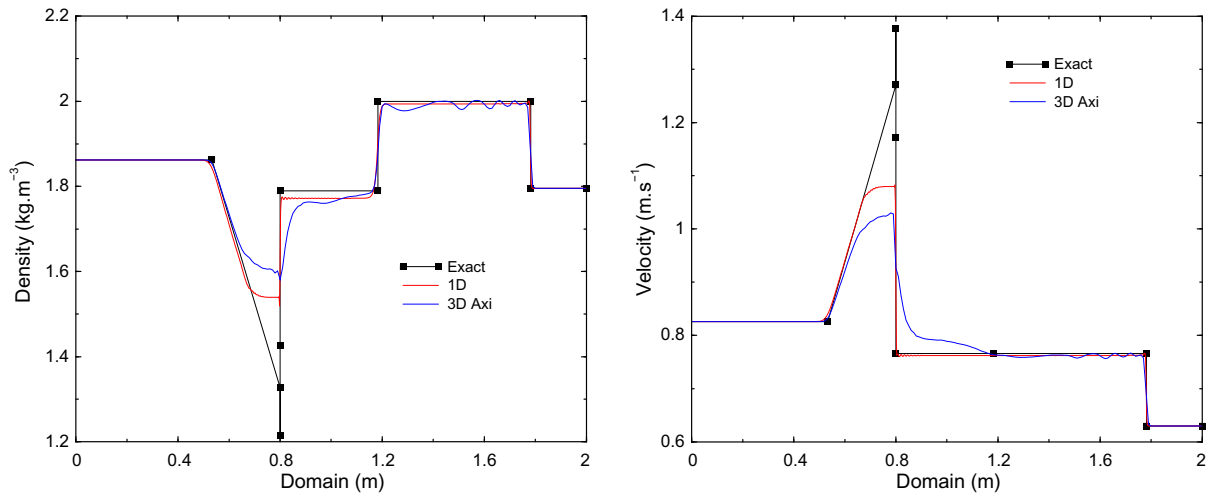
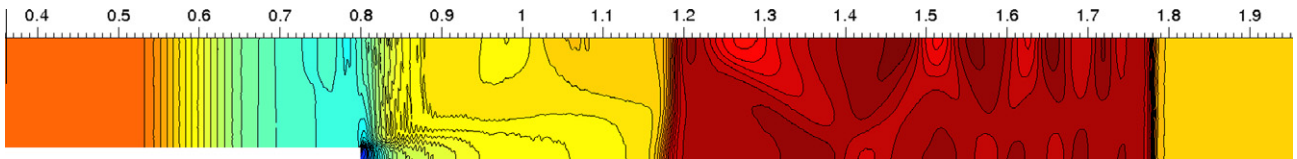**Fig. 37.** Configuration of type $LRR_1 = \{1 - r, 0 - w, 1 - s, 0 - w, 2 - w, 3 - s\}$ at time 0.5 s.

Fig. 38. Fifty isodensity from 1.3 to 2 at time 0.5 s.

Table 16
Configuration of type $LRR_3 = \{1 - s, 2 - w, 3 - r, 0 - w, 3 - s, 0 - w\}$.

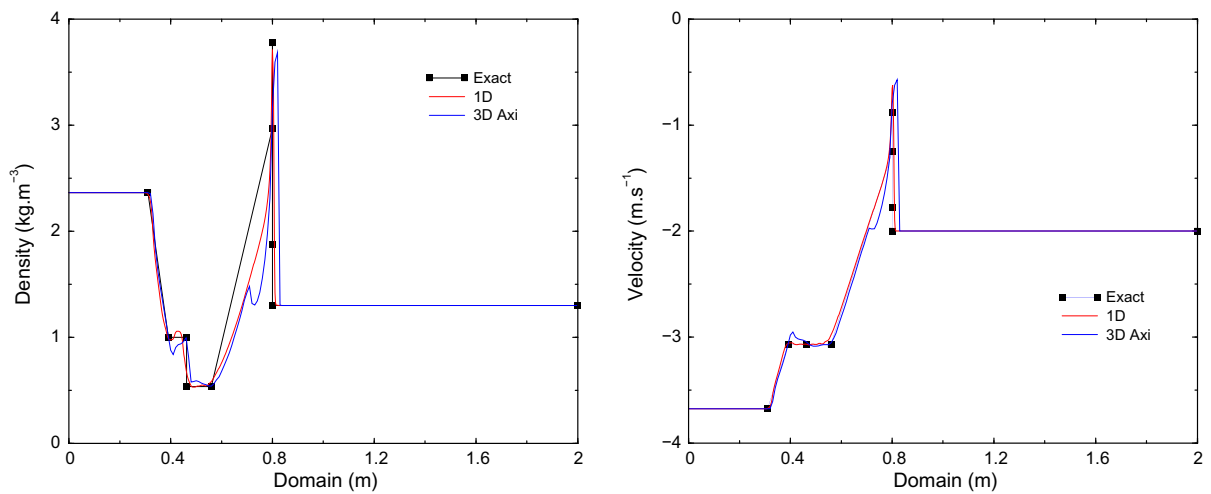|	ϕ	ρ (kg m^{-3})	u (m s^{-1})	P (Pa)	Mach
V_L	0.7	2.363115	−3.675948	1.0	4.775818
V_a	0.7	1.0	−3.067818	0.3	4.733745
V_b	0.7	0.533582	−3.067818	0.3	3.457843
V_l	0.7	2.969906	−1.250641	3.318027	1.0
$V_{s,l}$	0.78177	3.775791	−0.880818	4.643562	0.671275
$V_{s,r}$	0.78177	1.872903	−1.775738	1.667250	1.590641
V_R	1.0	1.3	−2	1	1.927248

Fig. 39. Configuration of type $LRR_3 = \{1 - s, 2 - w, 3 - r, 0 - w, 3 - s, 0 - w\}$ at time 0.12 s.
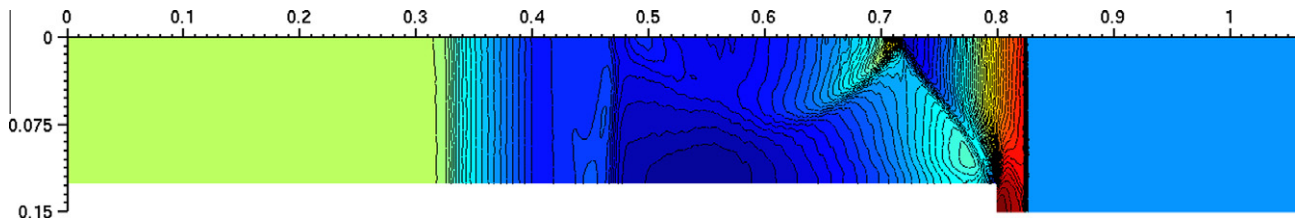
Fig. 40. Fifty isodensity from 1.6 to 5.2 at time 0.12 s.

4.4.2. Configuration LRR₃

Comments. The present test LRR_3 and the following case RRR_1 are performed to check that the couple of configurations (LRR_3, RRR_1) are symmetric in the following sense. Let V_L and V_R two states which provide a LRR_3 configuration for the Riemann problem. Let us choose the new initial condition such that $\widetilde{V}_R = V_L$ and $\widetilde{V}_L = V_R$ and change the velocity sign. Then we obtain a RRR_1 configuration which is symmetric to the LRR_3 with respect to the initial discontinuity location and the change of sign for the velocity.

Table 16 gives the exact solution obtained with the inverse Riemann problem while Figs. 39 and 40 show respectively the comparison between the exact solution and the numerical approximations for the density and velocity with the two schemes at time

Table 17
Configuration of type $RRR_1 = \{0 - w, 1 - s, 0 - w, 1 - r, 2 - w, 3 - r\}$.

	ϕ	ρ	u	P	Mach
V_L	1.0	1.3	2.0	1.0	1.927248
$V_{s,l}$	0.78177	1.872903	1.775738	1.667250	1.590641
$V_{s,r}$	0.78177	3.775791	0.880818	4.643562	0.671275
V_r	0.7	2.969906	1.250641	3.318027	1.0
V_a	0.7	0.533582	3.067818	0.3	3.457843
V_b	0.7	1.0	3.067818	0.3	4.733745
V_R	0.7	2.363115	3.675948	1.0	4.775818

Fig. 41. Configuration of type $RRR_1 = \{0 - w, 1 - s, 0 - w, 1 - r, 2 - w, 3 - r\}$ at time 0.2 s.
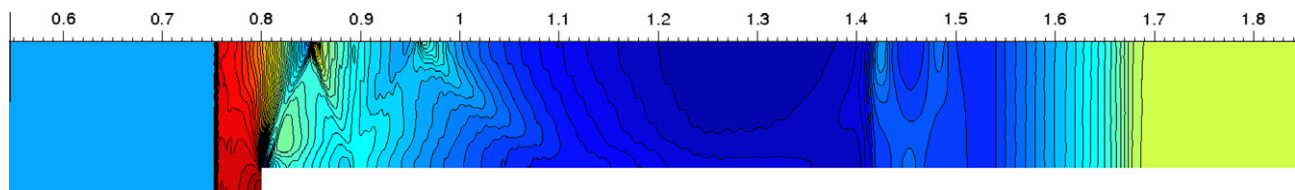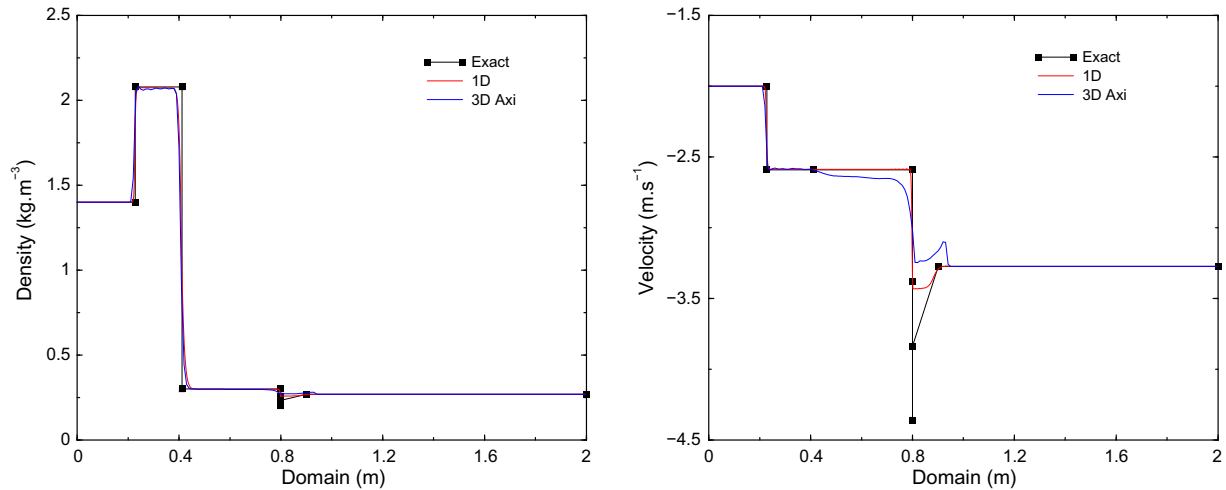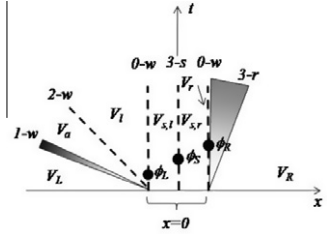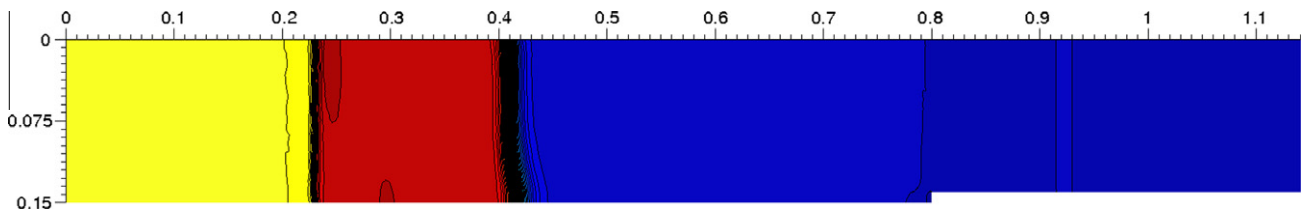

Fig. 42. Fifty isodensity from 0.3 to 4 at time 0.2 s.

Table 18
Configuration of type $RRR_3 = \{1 - s, 2 - w, 0 - w, 3 - s, 0 - w, 3 - r\}$.

	ϕ	ρ	u	P	Mach
V_L	1.0	1.4	−2.0	2.0	1.414214
V_a	1.0	2.077419	−2.591083	3.5	1.687118
V_l	1.0	0.3	−2.591083	3.5	0.641127
$V_{s,l}$	0.889412	0.258647	−3.379023	2.843740	0.861264
$V_{s,r}$	0.889412	0.200487	−4.359267	1.987030	1.170281
V_r	0.87	0.232799	−3.837976	2.449388	1.0
V_R	0.87	0.269081	−3.273959	3.0	0.828687

Fig. 43. Configuration of type $RRR_3 = \{1 - s, 2 - w, 0 - w, 3 - s, 0 - w, 3 - r\}$ at time 0.15 s.

Fig. 44. Fifty isodensity from 0.2 to 2.2 at time 0.15 s.

0.12 s. The figures have to be compared with the next configuration to check the symmetry. Note that the time is not the same for practical reasons since the LRR_3 configuration is outside of the interval [0,2] at time 0.2 s.

4.4.3. Configuration RRR_1

Comments. Table 17 gives the exact solution obtained with the inverse Riemann problem while Figs. 41 and 42 show respectively the comparison between the exact solution and the numerical approximations for the density and velocity with the two schemes. We first mention that we have drawn a simple line between V_r and V_a for the sake of simplicity to represent the rarefaction and the real curve would be a convex one very similar to the numerical approximations. For the present case, the intermediate value $V_{s,r}$ density is higher than the other density and we find again that both the numerical approximations try to catch the higher density value.

4.4.4. Configuration RRR_3

Comments. Table 18 gives the exact solution obtained with the inverse Riemann problem while Figs. 43 and 44 show respectively the comparison between the exact solution and the numerical

approximations for the density and velocity with the two schemes. The configuration RRR_3 is similar to the LRR_1 one (in particular the velocity). The $3 - r$ transition to the 3D sonic state at the interface is poorly approximated where this time the schemes attempt to catch the higher velocity between the three states $V_{s,l}$, $V_{s,r}$ and V_r. Density variations are too small to comment the simulations

Table 19
Configuration of types C and D.

	ϕ	ρ	u	P
Configuration of type $C = \{1 - s, 0 - w, 2 - w, 3 - s\}$				
V_L	0.8	0.2069	3.991	0.07
V_l	0.8	1.1109	0.3377	3.4634
V_r	0.3	1.0019	0.9985	2.9972
V_a	0.3	0.6997	0.9985	2.9972
V_R	0.3	0.1354	−3.1668	0.0833
Configuration of type $D = \{0 - w, 1 - s, 2 - w, 3 - s\}$				
V_L	0.8	0.2069	3.991	0.07
V_r	0.3	0.5736	3.8387	0.2918
V_a	0.3	2.4112	1.6389	3.934
V_b	0.3	0.724	1.6389	3.934
V_R	0.3	0.1354	−3.1668	0.0833

around the interface but the other states V_a, V_l are well-approximated.

5. Non uniqueness of the Riemann problem solutions

Non uniqueness of the Riemann problem solutions is well-known for the nonconservative Euler system [4] and the noncon-servative shallow-water problem [3]. The point is that the transition across the interface does not behave in the same manner whether we deal with a subsonic or a supersonic flow. Consequently, we can exhibit Riemann problems with two distinct entropy solutions (in the Lax sense) whether we use the subsonic branch of the interface transition or the supersonic one. We propose here several couples of configurations which are solutions
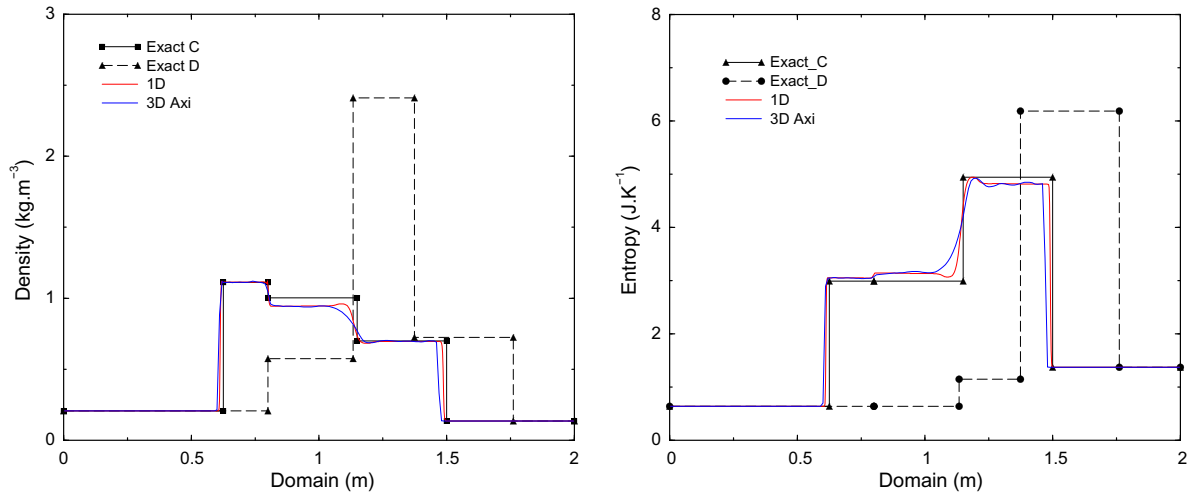

Fig. 45. Distribution of the density and the entropy obtained by the nonconservative and the axisymmetric models and the two solutions of the inverse Riemann problem at time t = 0.35 s.
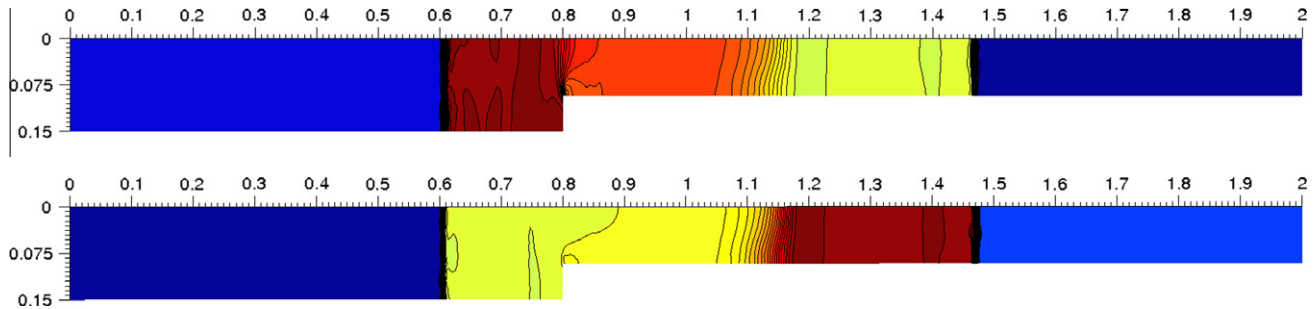

Fig. 46. Fifty isodensity (top) from 0.135 to 1.13 and 50 isoentropy (bottom) from 0.635 to 4.92 at time t = 0.35 s.
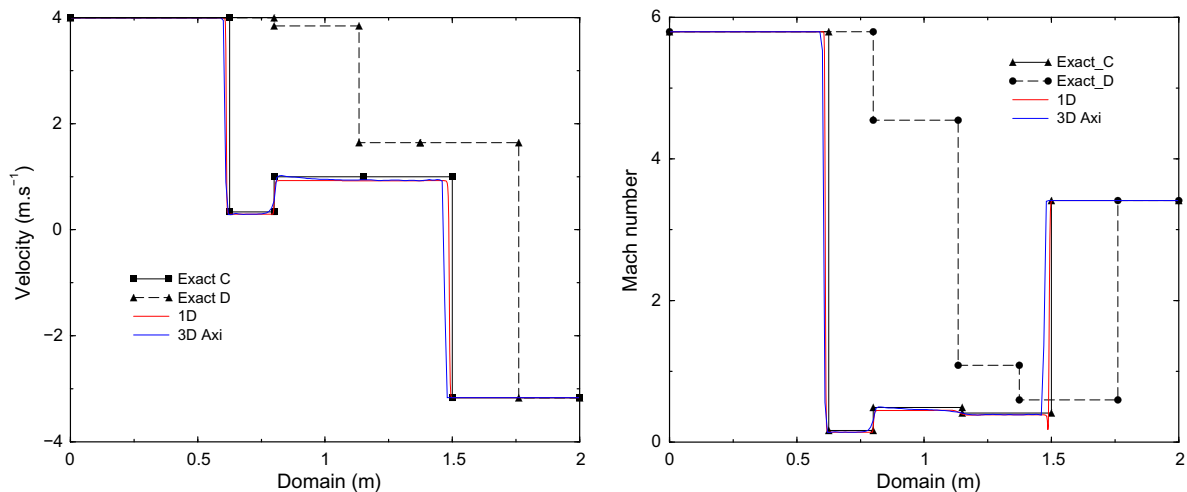

Fig. 47. Distribution of the velocity and the Mach number obtained by the nonconservative and the axisymmetric models and the two solutions of the inverse Riemann problem at time t = 0.35 s.
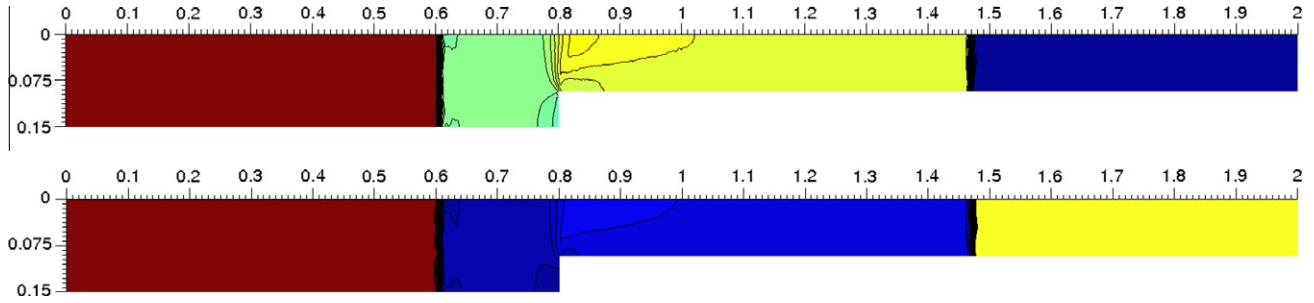
Fig. 48. Fifty isovelocity (top) from -3.17 to 3.99 and 50 isomach (bottom) from 0.0179 to 5.8 at time $t = 0.35$ s.

Table 20
Configuration of types D and RRR_1.

	ϕ	ρ (kg m^{-3})	u (m s^{-1})	P (Pa)
Configuration of type $D = \{0 - w, 1 - s, 2 - w, 3 - r\}$				
V_L	1.0	1	650	60,000
V_r	0.75	1.4557	595.3377	101502.1874
V_a	0.75	0.7469	790.5361	39874.3
V_b	0.75	4.9888	790.5361	39874.3
V_R	0.75	9.2747	860.373	95,000
Configuration of type $RRR_1 = \{0 - w, 1 - s, 0 - w, 1 - r, 2 - w, 3 - r\}$				
V_L	1.0	1	650	60,000
$V_{s,l}$	0.940495	1.0802	639.7901	66846.4501
$V_{s,r}$	0.940495	3.1490	219.4730	357338.2303
V_r	0.75	2.3128	374.7221	231970.8357
V_a	0.75	0.6589	790.7742	40,000
V_b	0.75	5	790.7742	40,000
V_R	0.75	9.2747	860.373	95,000

of the same Riemann problem and we compare the 1D-solution with the numerical approximation obtained with the axisymmetric model.

5.1. Non uniqueness between configurations C and D

We first test the configuration proposed by Andrianov and Warnecke in [4]. We have listed the densities, velocities and pressures obtained by the inverse Riemann problem in Table 19.

With the same initial conditions, the Riemann problem for the nonconservative model has two distinct entropy solutions in the Lax sense but the numerical scheme based on the nonconservative

Rusanov flux [13] and the numerical scheme based on the axisymmetric model provide the same configuration C. Fig. 45 gives the theoretical density and the entropy using the inverse Riemann problem and the numerical approximations obtained with the one-dimensional model and the axisymmetric model. We present in Fig. 46 the repartition of the density and entropy at the same time for the full three-dimensional model. We observe that shocks are longitudinal which guarantee a good correspondence between the one-dimensional nonconservative model and the three-dimensional conservative one.

We plot the velocity and the Mach number in Fig. 47 for the theoretical solutions (configuration C and D), the one-dimensional approximation and the axisymmetric model solution while we give in Fig. 48 the map of the velocity and the Mach number using the axisymmetric model. Like the density map, the velocity obtained by the axisymmetric model presents very straight longitudinal shocks which legitimate the one-dimensional approach.

5.2. Non uniqueness between configurations D and RRR1

We here propose a new non uniqueness case between configurations D and RRR_1. Densities, velocities and pressures for the two configurations obtained by the inverse Riemann problem are presented in Table 20.

With the same initial conditions, the Riemann problem for the nonconservative model has two distinct entropy solutions in the Lax sense but the numerical scheme based on the nonconservative Rusanov flux selects the D configuration whereas the numerical solution based on the axisymmetric model corresponds to the RRR_1 configuration. We display in Fig. 49 the theoretical density
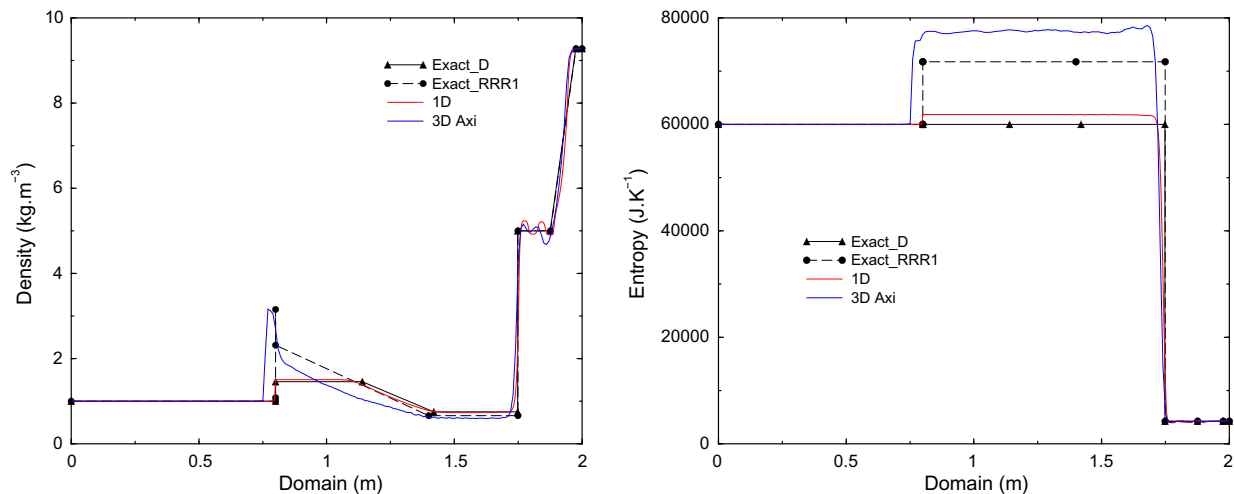

Fig. 49. Distribution of the density and the entropy obtained by the nonconservative and the axisymmetric models and the two solutions of the inverse Riemann problem at time $t = 1$ ms.
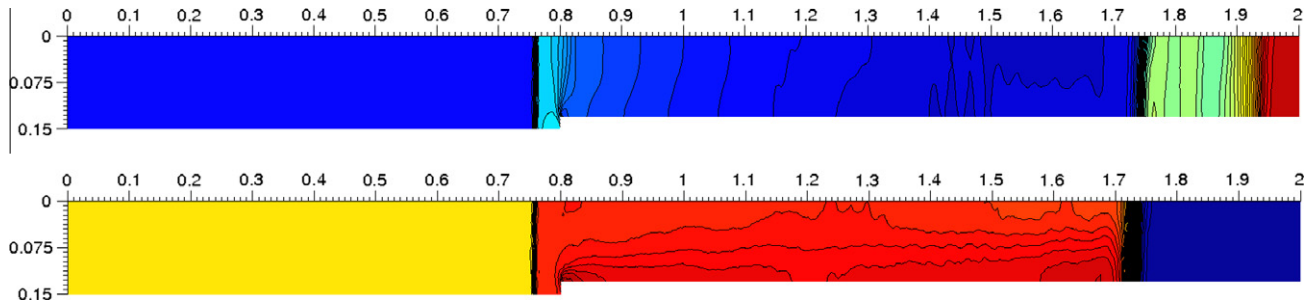
Fig. 50. Fifty isodensity (top) from 0 to 10 and 50 isoentropy (bottom) from 0 to 80,000 at time $t = 1$ ms.
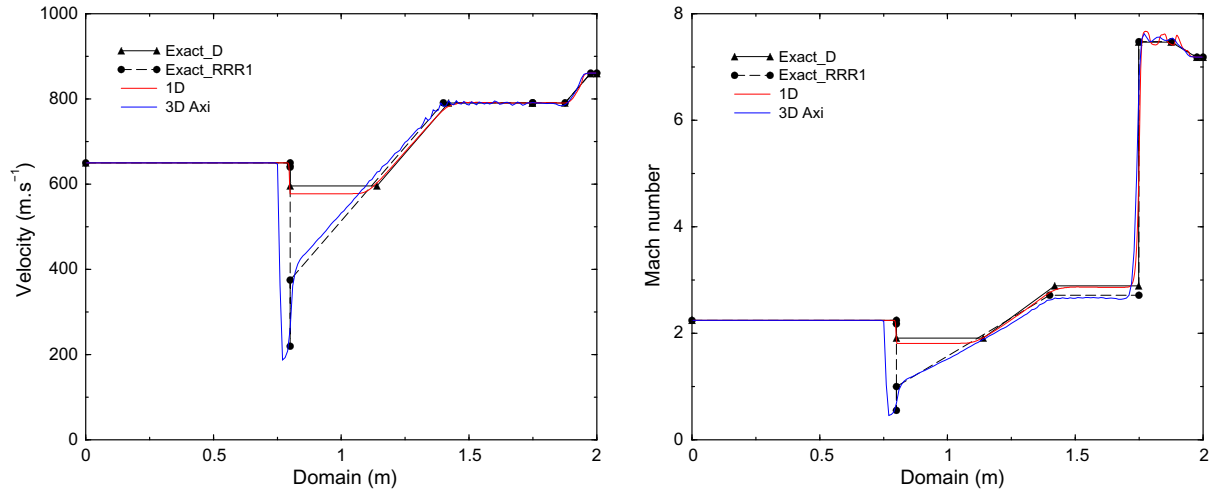

Fig. 51. Distribution of the velocity and the Mach number obtained by the nonconservative and the axisymmetric models and the two solutions of the inverse Riemann problem at time $t = 1$ ms.
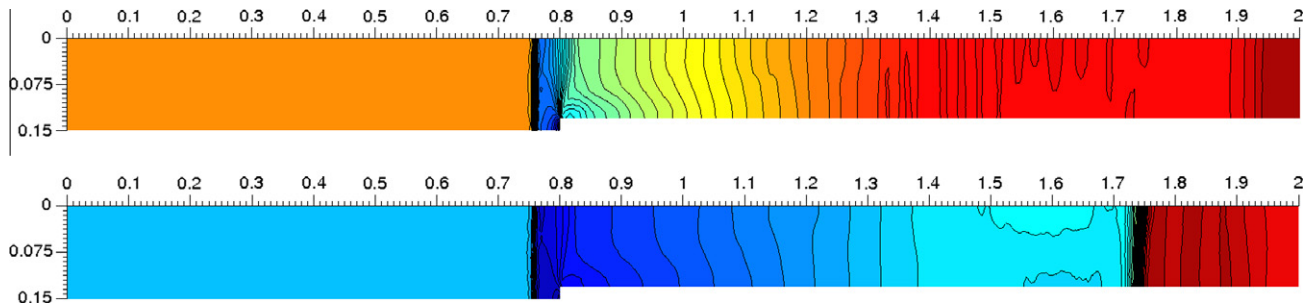

Fig. 52. Fifty isovelocity (top) from 0 to 900 and 50 isomach (bottom) from 0 to 8 at time $t = 1$ ms.
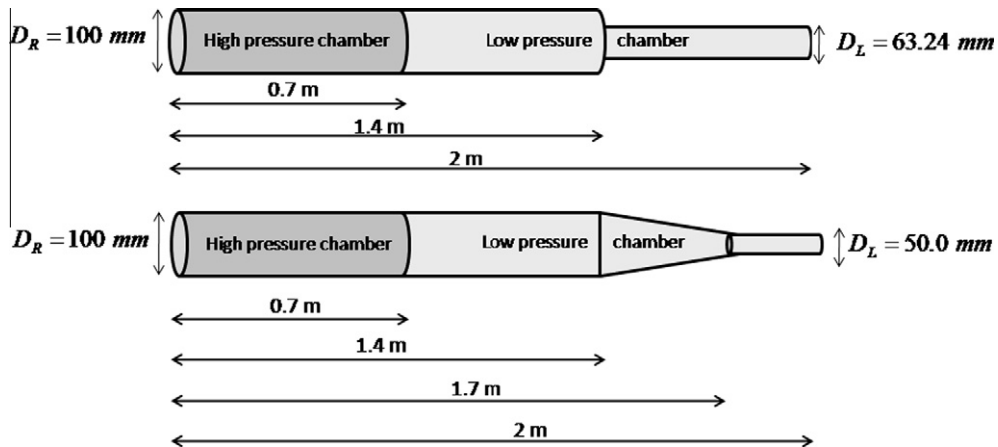

Fig. 53. Shock tube geometry for the test 1 (top) and test 2 (bottom).

Table 21
Initial conditions of the shock tube for the test 1.

Position (m)	ϕ	R (m)	ρ (kg m^{-3})	u (m s^{-1})	P (Pa)
$x = [0:0.7]$	1	0.05	35.6	0	30×10^5
$x = [0.7:1.4]$	1	0.05	1.1867	0	1×10^5
$x = [1.4:2]$	0.4	0.0316	1.1867	0	1×10^5

Table 22
Initial conditions of the shock tube for the test 2.

Position (m)	ϕ	R (m)	ρ (kg m^{-3})	u (m s^{-1})	P (Pa)
$x = [0:0.7]$	1	0.05	35.6	0	30×10^5
$x = [0.7:1.4]$	1	0.05	1.1867	0	1×10^5
$x = [1.4:1.7]$	$1 \rightarrow 0.25$	$0.05 \rightarrow 0.025$	1.1867	0	1×10^5
$x = [1.7:2]$	0.25	0.025	1.1867	0	1×10^5

and entropy using the inverse Riemann problem and the two numerical solutions with the one-dimensional and the axisymmetric models. We note that the physical solution obtained with the 3D-model corresponds to the largest global entropy production (global in the sense that we spatially integrate the entropy on interval [0,2]). Such a criterion has been mentioned by Andrianov and Warnecke [4].

We show in Fig. 50 the density and the entropy maps obtained with the axisymmetric model. We observe that the shocks are mainly longitudinal which explains the nice fitting between the numerical solution and configuration RRR_1.

We plot in Fig. 51 the velocity and the Mach number for the theoretical solutions for configurations D and RRR_1 and the numerical approximations using the 1D-nonconservative model and the 3D-conservative one. We observe a very good correspondence between the 1D-model and configuration D whereas the
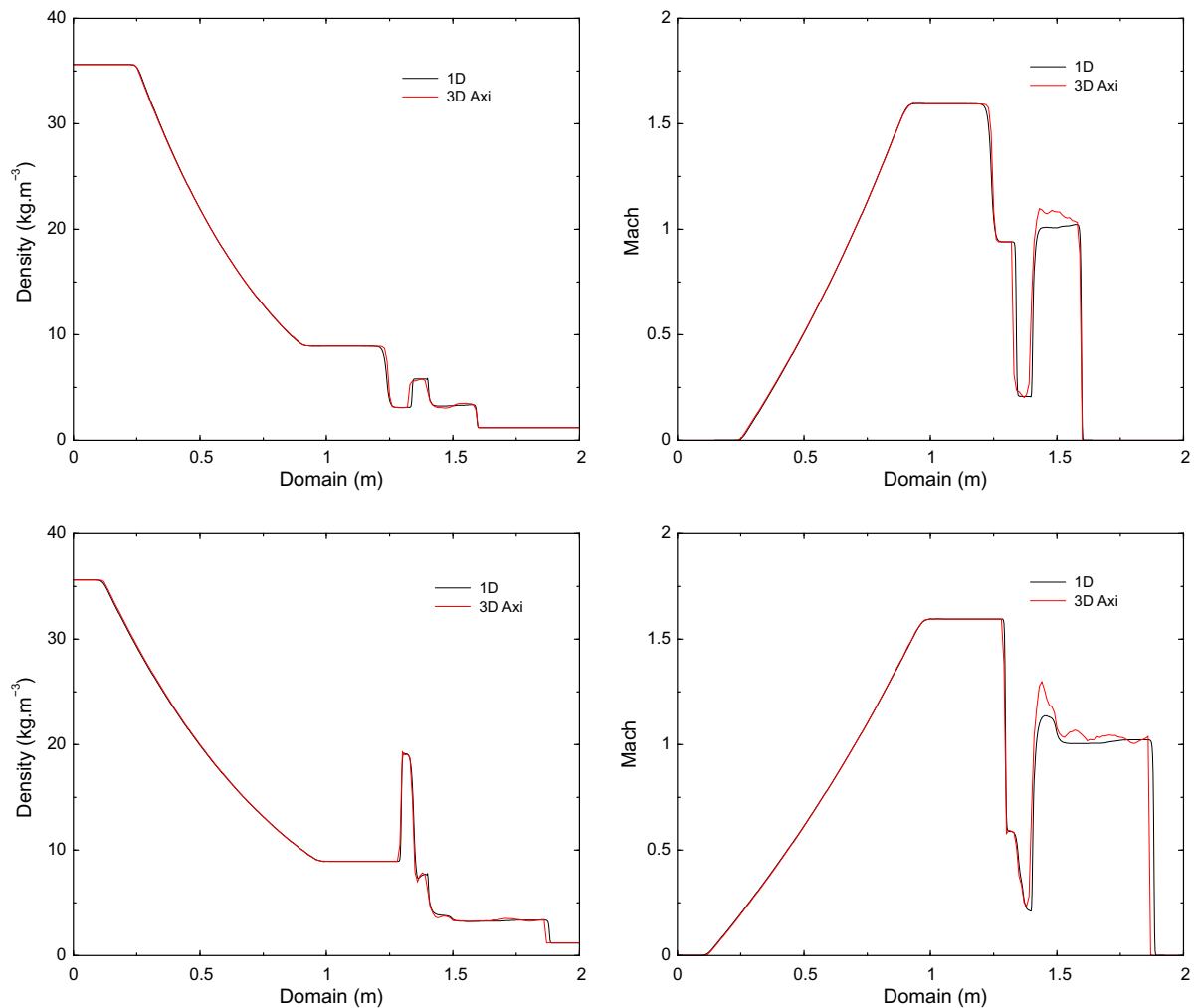
Fig. 54. Distribution of the density and the Mach number obtained by the two models at time t = 1.3 ms (top) and t = 1.7 ms (bottom) for the test 1.
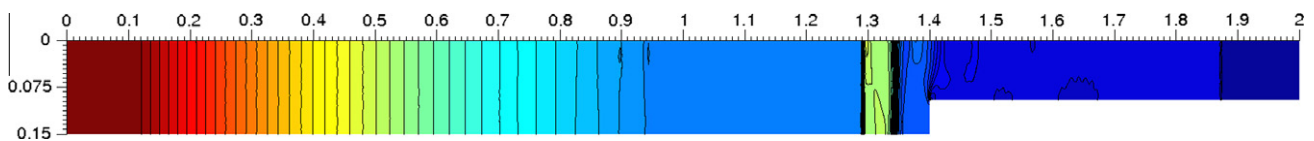
Fig. 55. Fifty isodensity from 1 to 36 at time t = 1.7 ms.

approximations obtained with the axisymmetric model suit well with configuration RRR_1.

Fig. 52 represents the velocity and Mach number maps at time $t = 1$ ms. Like the density and the entropy, shock waves are longitudinal which guarantees a good correspondence with the theoretical one-dimensional model.

6. Shock wave interaction with a cross-section reduction in a duct

In numerous engineering applications [6,28], practical situations do not exactly correspond to pure Riemann problems for the nonconservative Euler system with two definitively different states on the left and right side of a cross-section discontinuity. Indeed, in many applications, the state discontinuity and the cross-section jump are not located at the same place (see Fig. 53). A Riemann problem for the conservative Euler system generates travelling waves (an explosion generated by a high pressure and

a low pressure chambers separated by a diaphragm for instance) which interact with the cross-section jump located after the diaphragm. The incident shock wave is then separated into a transmitted shock wave and a reflected shock wave in function of the section variation.

In order to perform numerical simulations of such a situation, we consider a shock tube of length $x = [0:2]$ equipped with a section reduction situated at $x = 1.4$ m. The initial discontinuity between the high pressure chamber and the low pressure chamber is located at $x = 0.7$ m. As in the previous sections, we compare the waves evolution between the one-dimensional nonconservative model and the three-dimensional axisymmetric model. We have carried out two kinds of simulation whether we use a discontinuous or a smooth transition between the two sections as displayed in Fig. 53. We sum up here the two configurations we deal with. Note that the classical Riemann problem we use to generate the shock wave is exactly the same in the two situations in order to compare the transition effects.
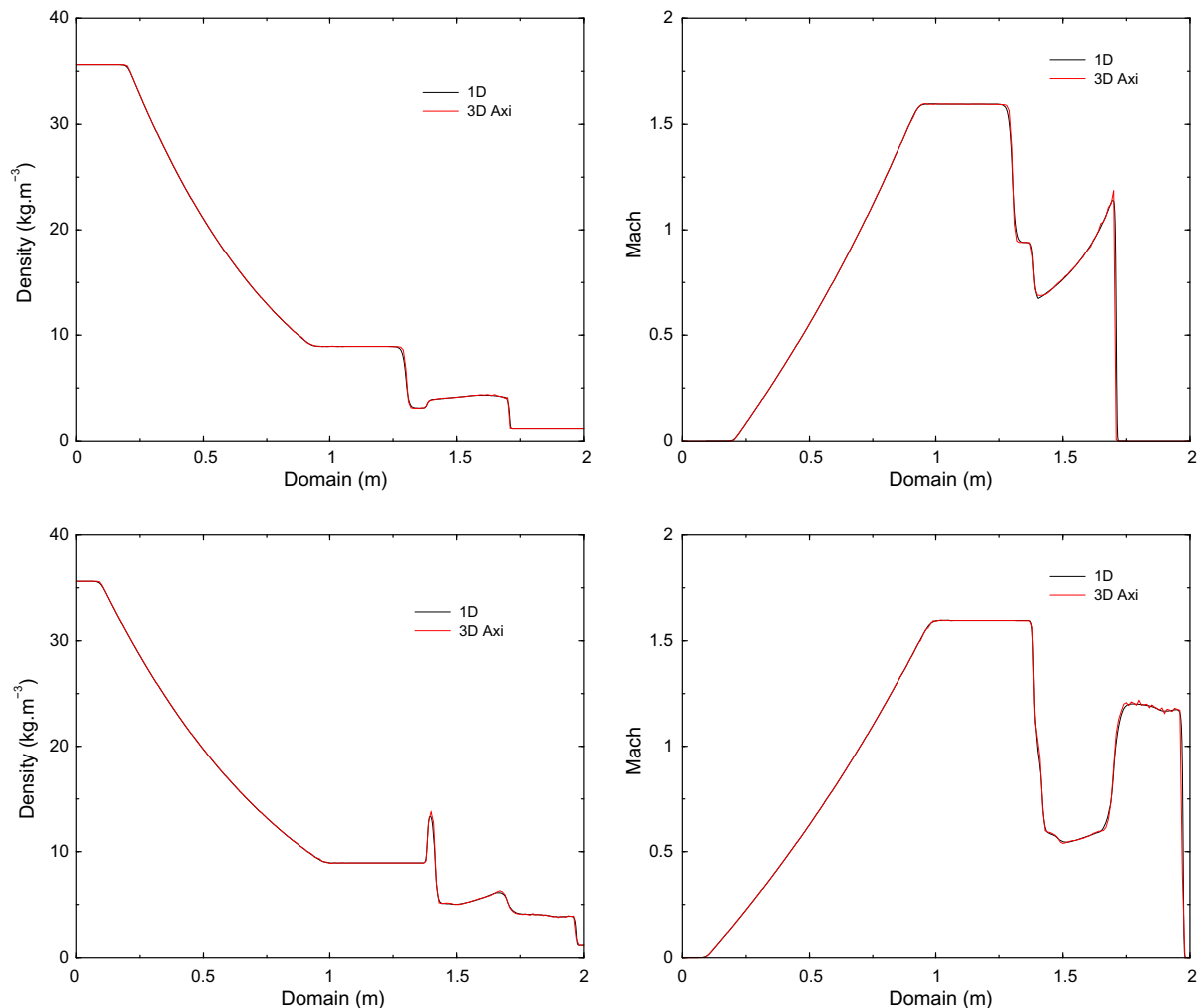
Fig. 56. Distribution of the density and the Mach number obtained by the two models at time $t = 1.45$ ms (top) and $t = 1.76$ ms (bottom) for the test 2.
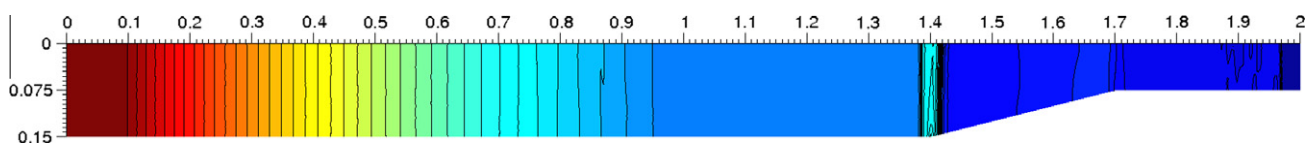
Fig. 57. Fifty isodensity from 1 to 36 at time $t = 1.76$ ms.

- A discontinuous cross-section reduction (test 1), *i.e.* an abrupt transition from $\phi = 1$ to $\phi = 0.4$ (respectively a change of cross-section from $R = 0.05$ to $R = 0.0316$ in the axisymmetric context). The initial conditions of the shock tube are summarized in Table 21.
- A regular cross-section reduction (test 2), *i.e.* corresponding to a linear transition from $\phi = 1$ to $\phi = 0.25$ (respectively a linear transition of the cross-section from $R = 0.05$ to $R = 0.025$). The initial conditions of the shock tube are summarized in Table 22.

6.1. The discontinuous transition case

We first consider the situation of the abrupt transition. Table 21 gives the initial conditions of the shock tube while Fig. 54 show respectively the comparison between the one-dimensional model and the axisymmetric one for the density and Mach number at two different times $t = 1.3$ ms (top) and $t = 1.7$ ms (bottom). At last, Fig. 55 gives the density isolines for the axisymmetric model at time $t = 1.7$ ms.

Comments. The incident shock wave generated by the Riemann problem is parted into a transmitted wave and a reflected wave at time $t = 1.3$ ms by the cross-section discontinuity located at $x = 1.4$ m. Both the models give a similar behaviour but several differences can be highlighted. We first observe that the nonconservative model generates a higher reflected wave density and a lower transmitted wave density with respect to the axisymmetric model. The transition between the cross-section discontinuity and the transmitted shock (the $3 - s$ shock) is also different: we note that the gas velocity increases just after the cross-section discontinuity for the axisymmetric model whereas the one-dimensional model presents a flat curve for the velocity. Nevertheless, we obtain a very good agreement between the two solutions, in particular the $3 - s$ shock corresponding to the transmitted wave is the same in the two simulations.

6.2. The smooth transition case

We now deal with the smooth transition case where we use the same Riemann problem to generate the incident wave. Table 22 gives the initial conditions of the shock tube while Fig. 56 show respectively the comparison between the one-dimensional model and the axisymmetric one for the density and Mach number at two different times $t = 1.45$ ms (top) and $t = 1.76$ ms (bottom). At last, Fig. 57 gives the density isolines for the axisymmetric model at time $t = 1.76$ ms.

Comments. With a regular cross-section variation, we obtain a perfect agreement between the two models even in the delicate zone situated after the position $x = 1.4$ m. Transitions between subsonic and supersonic states are also nice and, in this case, the one-dimensional nonconservative model is representative of the fully three-dimensional conservative one since there is no oblique wave generated by the cross-section variation. It is noticeable that the solution for regular variation situation is different to the abrupt one: the reflected and transmitted waves are smoothed and the intermediate states are different. For example, in the brutal variation case we observe a constant state just after the contact discontinuity $0 - w$ whereas the density increases linearly in the smooth variation case due to the linear variation of the cross-section.

7. Conclusion

A systematic comparison of all the admissible configurations between the one-dimensional nonconservative model and the axisymmetric conservative Euler system has been carried out. For the one-dimensional approach, we use the Rusanov flux adapted to the nonconservative Euler system proposed by Clain and Rochette [13] and the specific high-order scheme for the Euler system with cylindrical coordinates developed in [14]. Numerical results show a very good correspondence between the two models when the solutions of the axisymmetric model present straight longitudinal shocks, *i.e.* no noticeable transversal shock perturbs the solution. Simulations based on the axisymmetric model also confirm the existence of complex configurations such as the *LR, RR, LRR* and *RRR* configurations introduced in [13].

We have tested the example of non uniqueness proposed by Andrianov and Warnecke [4] and also proposed a new example of non uniqueness based on the D and RRR_1 configurations. Indeed, two entropy solutions in the Lax sense are available and we show that the numerical scheme for the one-dimensional nonconservative problem does not always pick up the same solution obtained by the axisymmetric model.

In the last section, we have proposed a representative situation of engineering applications where a strong shock wave, generated upstream, comes to propagate in a converging duct. Numerical results have shown a good agreement between the two models even if the cross-section transition is abrupt.

Acknowledgment

References

[1] Abgrall R, Saurel R. Discrete equations for physical and numerical compressible multiphase mixtures. J Comput Phys 2003;186:361–96.

[2] Alcrudo F, Benkhaldoun F. Exact solutions to the Riemann problem of the shallow water equations with a bottom step. Comput Fluids 2001;30(6): 643–71.

[3] Andrianov N. Performance of numerical methods on the non-unique solution to the Riemann problem for the shallow water equations. Int J Numer Meth Fluids 2005;47:825–31.

[4] Andrianov N, Warnecke G. On the solution to the Riemann problem for the compressible duct flow. SIAM J Appl Math 2004;64(3):878–901.

[5] Andrianov N, Warnecke G. The Riemann problem for the Baer–Nunziato two-phase flow model. J Comput Phys 2004;195:434–64.

[6] Britan A, Ben-Dor G, Igra O, Shapiro H. Shock waves attenuation by granular filters. Int J Multiphase Flow 2001;27(4):617–34.

[7] Berthon C, Nkonga B. Multifluid numerical approximation based on a multipressure formulation. Comput Fluids 2007;36:467–79.

[8] Bernetti R, Titarev VA, Toro EF. Exact solution of the Riemann problem for the shallow water equations with discontinuous bottom geometry. J Comput Phys 2008;227:3212–43.

[9] Buffard T, Clain S. Monoslope and multislope MUSCL methods for unstructured meshes. J Comput Phys 2010;229:3745–76.

[10] Castro Díaz MJ, Fernández-Nieto ED, Ferreiro AM. Sediment transport models in shallow-water equations and numerical approach by high order finite volume methodes. Comput Fluids 2008;37:299–316.

[11] Clain S, Clauzon V. The multislope MUSCL method. Proceeding in the finite volumes for complex application, vol. 5. Wiley; 2008.

[12] Chinnayya A, LeRoux AY, Seguin N. A well-balanced numerical scheme for shallow-water equations with topography: resonance phenomena. Int J Finite Volume 2004.

[13] Clain S, Rochette D. First- and second-order finite volume methods for the one-dimensional nonconservative Euler system. J Comput Phys 2009;228(22): 8214–48.

[14] Clain S, Rochette D, Touzani R. A multislope MUSCL method on unstructured meshes applied to compressible Euler equations for swirling flows. J Comput Phys 2010;229:4884–906.

[15] Désidéri JA, Goudjo A. Un schéma de volumes-finis décentré pour la résolution des équations d'Euler en axisymétrie. INRIA report no. 1005; 1989.

[16] Dumbser M, Castro M, Pares C, Toro EF. ADER schemes on ustructured meshes for nonconservative hyperbolic systems: applications to geophysical flows. Comput Fluids 2009;38:1731–46.

[17] Fernandez-Nieto ED, Marin J, Monnier J. Coupling superposed 1D and 2D shallow-water models: source terms in finite volume schemes. Comput Fluids 2010;39(6):1070–82.

[18] Garcia-Navarro P, Vazquez-Cendon ME. On numerical treatment of the source terms in the shallow water equations. Comput Fluids 2000;29(8 3):951–79.

[19] Gallouët T, Hérard J-M, Seguin N. Some approximate Godunov schemes to compute shallow-water equations with topography. Comput Fluids 2003;32: 479–513.

[20] Glaister P. Flux difference splitting for the Euler equations with axial symmetry. J Eng Math 1988;22:107–21.

[21] Goatin P, Le Floch PG. The Riemann problem for a class of resonant hyperbolic systems of balance laws. Ann l'Inst Henri Poincare (C) Non-Linear Anal 2004;21(6):881–902.

[22] Greenberg JM, Leroux AY. A well-balanced scheme for the numerical processing of source terms in hyperbolic equations. SIAM J Numer Anal 1996;33(1):1–16.

[23] Guardone A, Vigevano L. Finite element/volume solution to axisymmetric conservation laws. J Comput Phys 2007;224(2):489–518.

[24] Jacob PA. Transient, hypervelocity flow in an axisymmetric nozzle. ICASE report no 91-1, NASA Research Center; 1991.

[25] Leschziner MA, Rodi W. Computation of strongly swirling axisymmetric free jets. AIAA J 1984;22:1742–7.

[26] Parés C. Numerical methods for nonconservative hyperbolic systems: a theoritical framework. SIAM J Numer Anal 2006;44(1):300–21.

[27] Parés C, Castro M. On the well-balance property of Roe's method for nonconservative hyperbolic systems. Applications to shallow-water systems. ESAIM: Math Model Numer Anal 2004;38(5):821–52.

[28] Rochette D, Clain S, André P, Bussière W, Gentils F. Two-dimensional modelling of internal arc effects in an enclosed MV cell provided with a protection porous filter. J Phys D: Appl Phys 2007;40:3137–44.

[29] Rochette D, Clain S, Gentils F. Numerical investigations on the pressure wave and the gas cooling interacting with a porous filter, during an internal arc fault in medium voltage cells. IEEE Trans Power Deliv 2008;23(1):203–12.

[30] Rosatti G, Fraccarollo L. A well-balanced approach for flows over mobile-bed with high sediment-transport. J Comput Phys 2006;220:312–38.

[31] Saurel R, Abgrall R. A multiphase Godunov method for compressible multifluid and multiphase flow. J Comput Phys 1999;150:425–67.

[32] Zucrow MJ, Hoffman JD. Gas dynamics, vol. 2. John Wiley & Sons; 1977.